Computational and Theoretical Analysis of Electron Plasma Cooling by Resonant Interaction with a Microwave Cavity

E. Kur,[1, a)] F. Robicheaux,[2, b)] N. Evetts,[3] J. Fajans,[1] A. Guerra IV,[1] W. N. Hardy,[3] E. D. Hunter,[1] Z.T. Schroeder,[2] and J. S. Wurtele[1]

[1)]*Department of Physics, University of California, Berkeley, California, 94720 USA*

[2)]*Department of Physics and Astronomy, Purdue University, West Lafayette, Indiana 47907, USA*

[3)]*Department of Physics, University of British Columbia, V6T 1Z4 Canada*

(Dated: June 28, 2020)

Recent experiments demonstrated that the cyclotron cooling rate of an electron plasma in a Penning-Malmberg trap can be increased by placing the plasma in a cavity and adjusting the magnetic field to make the cyclotron motion resonant with a cavity mode. Here this physics is studied with a coupled oscillator model and analyzed both analytically and numerically. Plasma cooling performance is evaluated over a wide range of system parameters, including the number of electrons, the coupling to the local electric field, the magnetic field gradient, and the detuning between the cavity and cyclotron frequencies. Scaling the equations shows that the system is well-described by a few key dimensionless quantities.

PACS numbers: random 32.80.Ee, 34.20.Cf, 37.10.Jk

I. INTRODUCTION

Cold nonneutral lepton plasmas are employed in a wide range of applications[1]. Some of these applications, such as antihydrogen synthesis[2], require temperatures in the low tens of Kelvin. The steady-state temperature of these trapped plasmas is determined by the balance between heating (which arises from external noise sources, the temperature of the confinement environment[3], and plasma expansion) and cooling (from energy radiated away through the cyclotron emission). Except at the lowest temperatures[4], collisions between the charged particles in the plasma rapidly equilibrate the perpendicular and parallel temperatures[5]. In the absence of a heating mechanism, the plasma would thus come into thermal equilibrium with the black body radiation of its environment, but with heating the equilibrium temperature is higher[6]. A simplistic but useful model yields $T_{eq} = T_0 + H/\gamma$, where T_0 is the environment temperature, H is the heating rate, and the radiative energy loss rate for electrons is $\gamma = 0.26\,B^2\ \mathrm{s}^{-1}$ when B is in Tesla. If the rate of radiative loss can be increased, then the effects of any heating sources H can be concomitantly reduced. One method, which is impractical beyond a few Tesla is to increase the magnetic field. Another is to utilize the Purcell effect, placing the plasma in a microwave cavity where a mode is resonant with the cyclotron frequency, as first proposed by O'Neil[7] in 1980.

The original discussion of the Purcell effect[8] concerned the nuclear magnetic resonance of nuclear spins in a cavity. One way to think of this system is that the cavity concentrates the electromagnetic modes to a small range of frequencies, enhancing the relaxation rate. The corresponding electron cyclotron resonance with one electron in a cavity has been carefully studied[9]. The cavity plus one electron can be thought of as two coupled oscillators one of which, the cavity, is more highly damped; the interaction between the cavity and the nearly undamped cyclotron motion causes energy to flow from the cyclotron motion to the cavity, where the energy is lost by damping. The plasma case[7] is analogous to having multiple oscillators. They all interact with a single cavity mode, which couples their dynamics and facilitates rapid transfer between the electron cyclotron motion and the cavity.

The first experimental verification came in 2015, where enhanced cooling was demonstrated[6] for low numbers of plasma electrons ($< 10^6$). The plasma was kept in a Penning-Malmbeg trap, with the walls of the trap slightly bulged to produce an effective cavity[10] with $Q \sim 1000$. In these experiments significant enhancement over free-space cooling was obtained (factor of 10 or more). Subsequent experiments[11,12] further explored the efficacy of plasma cavity cooling as a function of particle number and magnetic field gradient, and demonstrated cooling for particle numbers approaching 10^8.

While the theory for one electron interacting with a cavity mode is well understood, Ref. 6 found several counterintuitive results for the many-electron case. For example, the single electron rate is larger the closer the electron is to an antinode of the cavity mode, yet Ref. 6 found the radiative decay rate was often largest when the plasma was trapped at a node of the cavity mode. Furthermore, the cooling rate decreased as the number of electrons increased, well before the cavity was overloaded (the cavity temperature remained comparable to or below the plasma temperature).

We describe a simplified model for treating this system and perform calculations in several limits of the plasma parameters. The simplified model is cast as a set of coupled, damped oscillators with the oscillation amplitude scaled so that the cyclotron motion and the cavity oscillation are treated on the same footing. We describe how the parameters in the simplified model are related to physical parameters in an experiment and how to incorporate features like a spatially dependent magnetic field, spatially dependent coupling to the cav-

[a)]Electronic mail: k-gene@berkeley.edu
[b)]Electronic mail: robichf@purdue.edu

ity mode, and collisions with background neutrals. We also describe how to modify the equations to treat plasmas with millions of electrons using only a few thousand representative electrons. In the limit that the fastest rate in the system is the cavity decay rate, we give a set of rate equations involving 4 coupled temperatures. In all examples, we give a physical description for the behavior of the plasma.

This paper is organized as follows. In Sec. II we derive the coupled oscillator model. In Sec. III the model is analyzed under the simplifying assumption that axial dynamics is not important. We find that the dynamics is described by a combination of single-electron and multi-electron effects, and we identify different regimes of cooling depending on ratios of an appropriately defined coupling strength to the cavity mode and the frequencies $N\Gamma_1$, Γ, $\delta\Omega$, and Δ. Here Γ_1 is the single-electron decay rate at a cavity resonance, Γ is the cavity mode decay rate, $\delta\Omega$ is the spread in electron detuning and Δ is the mean detuning between the electron cyclotron motion in the plasma and the cavity mode. Comparisons with numerical simulation are provided in Sec. IV. The case of axially bouncing electrons is considered in Sec. V and collisions are briefly considered in Sec. VI. Conclusions are presented in Sec. VII.

II. BASICS OF MULTI-ELECTRON INTERACTIONS WITH RESONANT CAVITY

In this section we derive equations describing the interaction of a cavity mode with electrons located near the axis of the cavity. Our main result of the paper is the set of Eqs. (8), which provide a tractable description of plasma cooling in a cavity. These come from Maxwell's equations and the Lorentz force law, with approximations made to model a regime typical of magnetized plasma experiments.

We begin by writing the vector potential $\boldsymbol{A}_{\rm cav}(\boldsymbol{x},t)$ for a TE radiation field (a similar analysis holds for TM fields) inside a cylindrical resonant cavity as

$$\boldsymbol{A}_{\rm cav}(\boldsymbol{x},t) = \frac{m_e c}{e}\sum_{\alpha,\lambda} a_\alpha^{[\lambda]}(t)\boldsymbol{h}_\alpha^{[\lambda]}(\boldsymbol{x})\exp(-i\omega_\alpha t) + \text{c.c.}. \quad (1)$$

The electron mass, electron charge, and speed of light are m_e, e, and c respectively. Here $\alpha = \{mnp\}$ is the mode (multi)index, $a_\alpha^{[\lambda]}$ is the dimensionless mode amplitude, $\boldsymbol{h}_\alpha^{[\lambda]}$ is the dimensionless mode function, ω_α is the normal mode frequency, and $\lambda = 1,2$ labels the degeneracy, as needed (the $m \neq 0$ TE$_{mnp}$ modes are doubly-degenerate in a cavity with perfect azimuthal symmetry). We use the normalization $\max(|\boldsymbol{h}_\alpha^{[\lambda]}|) = 1$ for the mode function $\boldsymbol{h}$ and define the effective mode volume V_α through

$$\int \mathrm{d}^3\boldsymbol{x}\, \boldsymbol{h}_{\alpha'}^{[\lambda']*}\cdot\boldsymbol{h}_\alpha^{[\lambda]} = V_\alpha\delta_{\alpha'\alpha}\delta_{\lambda'\lambda}, \quad (2)$$

where $\delta_{\mu\mu'} = 1$ when $\mu = \mu'$ and 0 otherwise.

We couple the cavity field (1) to a collection of N electrons, with the jth electron having position $\boldsymbol{x}_j(t)$ and velocity $\boldsymbol{v}_j(t)$. We assume there is an additional (external) axial, nearly-uniform magnetic field $\boldsymbol{B}_{\rm ext} = B\hat{\boldsymbol{z}}$ that sets the electron cyclotron frequencies $\Omega_j = e|\boldsymbol{B}_{\rm ext}(\boldsymbol{x}_j)|/m_e$ and provides radial confinement. We model inhomogeneities in $\boldsymbol{B}_{\rm ext}$ with position-dependent cyclotron frequencies, so different electrons will generally have different Ω_j. Axial confinement is provided by an external electric field $\boldsymbol{E}_{\rm ext}(\boldsymbol{x},t) = E(z)\hat{\boldsymbol{z}}$. The coupled system obtained from Maxwell's equations and the Lorentz force law is

$$\begin{aligned}-\nabla^2\boldsymbol{A}_{\rm cav}(\boldsymbol{x},t) + \frac{1}{c^2}\frac{\partial^2\boldsymbol{A}_{\rm cav}(\boldsymbol{x},t)}{\partial t^2} &= \mu_0\boldsymbol{J}(\boldsymbol{x},t)\\ &= -e\mu_0\sum_j \boldsymbol{v}_j(t)\delta(\boldsymbol{x}-\boldsymbol{x}_j(t)),\end{aligned} \quad (3a)$$

$$\dot{\boldsymbol{v}}_j = -\frac{e}{m_e}\left[\boldsymbol{v}_j\times\boldsymbol{B}_{\rm ext} + \boldsymbol{E}_{\rm cav}(\boldsymbol{x}_j,t) + \boldsymbol{E}_{\rm ext}(\boldsymbol{x}_j,t)\right], \quad (3b)$$

where $\boldsymbol{E}_{\rm cav} = -\partial\boldsymbol{A}_{\rm cav}/\partial t$ is the cavity electric field, we disregard the cavity magnetic field in Eq. (3b) as its effect on the electron motion is negligible compared to the effects of $\boldsymbol{B}_{\rm ext}$ and $\boldsymbol{E}_{\rm cav}$, and we neglect any direct interactions between the electrons (though accounting for the electrostatic mean self-fields would require only minor modifications to the above equations).

To simplify the coupling equations, we first substitute (1) into (3), then use the eikonal approximation $|\dot{a}/a| \ll \omega, |\ddot{a}/\dot{a}| \ll \omega$ and introduce the spherical basis $\hat{\boldsymbol{e}}_\pm = (\pm\hat{\boldsymbol{x}} - i\hat{\boldsymbol{y}})/\sqrt{2}$, $\hat{\boldsymbol{e}}_0 = \hat{\boldsymbol{z}}$. Recall that a vector written in the spherical basis $\boldsymbol{v} = \sum v_m\hat{\boldsymbol{e}}_m$ has components $v_m = \hat{\boldsymbol{e}}_m^*\cdot\boldsymbol{v}$ and in particular $v_\pm = (\pm v_x + iv_y)/\sqrt{2}$. We assume the frequency spacing of cavity modes is large enough that electrons will only be resonant with a single (degenerate) cavity mode, decoupling all other modes from our equations. We thus omit the mode indices for clarity.

We factor out the dominant oscillation in the system by defining $\bar{a}$ via $\bar{a}\exp\left(-i\bar{\Omega}t\right) = a\exp\left(-i\omega t\right)$ and define $\bar{v}_{j\pm} \equiv v_{j\pm}\exp\left(\mp i\bar{\Omega}t\right)$, where $\bar{\Omega} \equiv \sum_j\Omega_j/N$ is the average cyclotron frequency of the electrons. We discard any remaining fast (non-resonant) oscillations using the rotating wave approximation, leaving

$$\dot{\bar{a}}^{[1]} = \left(i\Delta - \frac{\Gamma}{2}\right)\bar{a}^{[1]} - \frac{i\mu_0 e^2 c}{2m_e\omega V}\sum_j \bar{v}_{j-}h_-^{*[1]}(\boldsymbol{x}_j), \quad (4a)$$

$$\dot{\bar{a}}^{[2]} = \left(i\Delta - \frac{\Gamma}{2}\right)\bar{a}^{[2]} - \frac{i\mu_0 e^2 c}{2m_e\omega V}\sum_j \bar{v}_{j-}h_-^{*[2]}(\boldsymbol{x}_j), \quad (4b)$$

$$\dot{\bar{v}}_{j-} = \left(-i\Delta_j - \frac{\gamma}{2}\right)\bar{v}_{j-} - i\omega c\left[\bar{a}^{[1]}h_-^{[1]}(\boldsymbol{x}_j) + \bar{a}^{[2]}h_-^{[2]}(\boldsymbol{x}_j)\right], \quad (4c)$$

$$\dot{v}_{jz} = -eE(\boldsymbol{x}_j)/m_e, \quad (4d)$$

where $\Delta \equiv \bar{\Omega} - \omega$ is the detuning of the average cyclotron frequency from the cavity, $\Delta_j \equiv \Omega_j - \bar{\Omega}$ are the detunings of the individual cyclotron frequencies from the average cyclotron frequency, $\Gamma = \omega/Q$ is a damping introduced to model resistive losses in the cavity walls (Q denotes the Q-factor of the cavity), γ is a damping introduced to model coupling to

traveling wave modes that leave the cavity (since our cavities are embedded within waveguides), and $\boldsymbol{x}_j = \boldsymbol{x}_j(t)$ is the time-dependent position of electron j. The equations for $\bar{v}_{j+}$ follow from $\bar{v}_{j+} = -\bar{v}^*_{j-}$. See table I for a summary of notation and definitions. The terms that have been dropped are counter-rotating, oscillating like $\exp(2i\omega t)$, and they contribute corrections of order $\Delta/\omega, \Gamma/\omega$ or smaller. Dropping them is valid so long as ω and the Ω_j are larger than any other frequency scale in the system. We assume that the cyclotron radius is smaller than any other length scale, so that $h_\pm(\boldsymbol{x}_j)$ can be evaluated at the center of the cyclotron orbit (guiding center) of the jth electron.

In accordance with experiment, we take the plasma to be near the axis of the cavity. Thus, the guiding centers have radial coordinates ρ_j satisfying $\rho_j/\rho_{\text{cav}} \ll 1$, where ρ_{cav} is the radius of the cavity. We can take linear combinations of the degenerate modes so that near the axis the new modes are almost completely left/right circularly polarized. We can then choose a labeling convention such that $h^{[1]}_+(\rho \ll \rho_{\text{cav}}), h^{[2]}_-(\rho \ll \rho_{\text{cav}}) \sim (\rho/\rho_{\text{cav}})^2 \approx 0$, hence the $\lambda = 2$ mode approximately decouples and leaves

$$\dot{\bar{a}} = \left(i\Delta - \frac{\Gamma}{2}\right)\bar{a} - \frac{i\mu_0 e^2 c}{2m_e\omega V}\sum_j \bar{v}_{j-} h^*_-(\boldsymbol{x}_j), \tag{5a}$$

$$\dot{\bar{v}}_{j-} = \left(-i\Delta_j - \frac{\gamma}{2}\right)\bar{v}_{j-} - i\omega c h_-(\boldsymbol{x}_j)\,\bar{a}, \tag{5b}$$

$$\dot{v}_{jz} = -eE(\boldsymbol{x}_j)/m_e, \tag{5c}$$

where we have dropped the degeneracy labels.

Lastly, we introduce oscillator variables

$$b_0 \equiv \bar{a}, \tag{6a}$$

$$b_j \equiv \frac{e}{\omega c\sqrt{2m_e V\varepsilon_0}}\,\bar{v}_{j-}, \tag{6b}$$

which make Eqs. (5) more symmetrical:

$$i\dot{b}_0 = -\left(\Delta + i\frac{\Gamma}{2}\right)b_0 + \sum_j b_j\eta^*_j, \tag{7a}$$

$$i\dot{b}_j = \left(\Delta_j - i\frac{\gamma}{2}\right)b_j + b_0\eta_j, \tag{7b}$$

$$\dot{v}_{jz} = -eE(\boldsymbol{x}_j)/m_e, \tag{7c}$$

with $\eta_j = eh_-(\boldsymbol{x}_j)/\sqrt{2m_e V\varepsilon_0}$. Once the external electric field is specified, Eq. (7c) can be solved for $z_j(t)$, which gives the axial motion of the guiding centers. Substituting the solution back into Eqs. (7a)-(7b) leaves

$$i\dot{b}_0 = -\left(\Delta + i\frac{\Gamma}{2}\right)b_0 + \sum_j b_j\eta^*_j(t), \tag{8a}$$

$$i\dot{b}_j = \left(\Delta_j(t) - i\frac{\gamma}{2}\right)b_j + b_0\eta_j(t), \tag{8b}$$

with the guiding center motion providing the time-dependence of η_j and Ω_j. In the rest of the paper, we detail the implications of Eqs. (8) for plasma cooling via electron cyclotron radiation. From the definitions above, the electron kinetic energy (which we use as a proxy for the plasma temperature) is proportional to $\sum_j |b_j|^2$. Solving (8) for $b_j(t)$ thus allows us to determine the cooling rate of the plasma.

Eqs. (8) are linear in the (complex) oscillator amplitudes, so the system may be regarded as a type of Schrödinger equation $i\mathrm{d}|b\rangle/\mathrm{d}t = M(t)|b\rangle$. The frequency η couples the (cavity and plasma) oscillators and plays a role similar to the Rabi frequency, setting the timescale for energy exchange between the cavity and the plasma (in the absence of dissipation). Alternatively we can view Eqs. (8) as a collection of $(N+1)$ oscillators with a special type of non-local coupling (all oscillators coupled to one). See Refs. 13–23 for other applications of such coupled oscillator systems. Lastly we note that a similar formalism (with appropriate adjustments to Γ, η, etc.) can be used to model other cooling mechanisms[24] (such as resistive cooling). For example, if we wish to apply our formalism to ion cooling it may be impractical to use cyclotron cooling since having a cavity mode resonant at the ion cyclotron frequency requires a very large cavity. However, we can reinterpret η as a cavity-plasma coupling strength resulting from an appropriate alternative cooling mechanism thereby allowing a similar analysis (with equations similar to (8)) for non-cyclotron cooling.

III. CAVITY INTERACTION WITH AXIALLY STATIONARY ELECTRONS: THEORETICAL CONSIDERATIONS

A. Introduction

We first analyze Eqs. (8) in the absence of axial motion. This fixes the guiding centers in place (equivalent to setting $E_{\text{ext}} \approx 0$ and initializing the electrons with no axial velocity) and gives each electron its own time-independent Ω_j, which results in a time-independent M. The solution for the oscillators is thus $|b(t)\rangle = \exp(-iMt)\,|b(0)\rangle$. Solving the system is reduced to diagonalizing M. In this section, we analytically solve the system for the case of a single electron and the case of many electrons with identical cyclotron frequencies. Then we introduce the theoretical framework for understanding the numerical simulations of many electrons with detuning (Sec. IV). Though in practice, electrons will always have axial motion, key features of plasma cooling can be understood without including axial motion, so we postpone discussion of its additional effects to Sec. V.

B. Behavior of a Single Electron

For a single electron, we expect enhanced radiative power loss from coupling to the cavity due to the Purcell effect. [8] We reproduce the calculations here using our notation. Note that with only one electron, $\Omega_1 = \bar{\Omega} \equiv \Omega$ and thus $\Delta_1 = 0$. Eqs. (8)

become

$$i\dot{b}_0 = -\left(\Delta + i\frac{\Gamma}{2}\right) b_0 + b_1\eta_1^*, \tag{9a}$$

$$i\dot{b}_1 = -i\frac{\gamma}{2} b_1 + b_0\eta_1. \tag{9b}$$

To find the decay rate, we look for eigenvalues of Eqs. (9) by substituting $b_0, b_1 \sim \exp(-i\alpha t)$. The complex frequency α satisfies the quadratic equation

$$\left(\alpha + i\frac{\gamma}{2}\right)\left(\alpha + \Delta + i\frac{\Gamma}{2}\right) = |\eta_1|^2. \tag{10}$$

It is instructive to examine the two solutions in the limit $\eta \ll \Gamma, \Delta$:

$$\alpha_1 \simeq -\Delta - i\frac{\Gamma}{2} - \frac{|\eta|^2}{\Delta + i(\Gamma-\gamma)/2}, \tag{11}$$

and

$$\alpha_2 \simeq -i\frac{\gamma}{2} + \frac{|\eta|^2}{\Delta + i(\Gamma-\gamma)/2}, \tag{12}$$

where α_1 corresponds to the mode where mainly the cavity is excited and α_2 corresponds to the mode where mainly the cyclotron motion is excited. We can discard γ from the denominators as $\Gamma \gg \gamma$ in the cases of interest. The two solutions

$$\alpha_1 \simeq -\Delta - \delta\omega - i\frac{\Gamma - \Gamma_1}{2}, \tag{13}$$

and

$$\alpha_2 \simeq +\delta\omega - i\frac{\gamma + \Gamma_1}{2}, \tag{14}$$

thus show a frequency shift

$$\delta\omega \equiv \frac{4|\eta|^2\Delta}{\Gamma^2[1 + (2\Delta/\Gamma)^2]}, \tag{15}$$

and a change in decay rate

$$\Gamma_1 \equiv \frac{4|\eta|^2}{\Gamma[1 + (2\Delta/\Gamma)^2]}. \tag{16}$$

The enhanced single-electron decay (16) offers a useful heuristic for optimizing cooling of plasmas with many electrons, since Γ_1 sets the cooling timescale even in the multi-electron case. For example, cooling is optimized when the average plasma cyclotron frequency is on resonance ($\Delta = 0$), when the plasma is at an anti-node (larger η), and at larger cavity Q (smaller Γ). Conversely, electrons with large detunings will not cool efficiently, so it is important to keep the cyclotron frequencies within the cavity linewidth.

C. Behavior of Many Electrons

We now turn to the case of many electrons interacting with the cavity. If the magnetic field is non-uniform, the cyclotron frequencies will have a spread

$$\delta\Omega^2 = \langle(\Omega - \bar{\Omega})^2\rangle. \tag{17}$$

Eq. (16) suggests we should couple all electrons on resonance and thus minimize $\delta\Omega$; however, coupling additional resonant electrons suppresses power loss, as only a single collective mode, the superradiant mode (Eqs. (18)), couples directly to the cavity. The superradiant mode experiences enhanced power loss, while the remaining subradiant modes mix into the superradiant mode in proportion to their detunings. In the limit of no detuning (uniform magnetic field), only the superradiant mode (containing $1/N$ of the total energy) will decay, leaving the electrons with most of their initial energy.

1. Uniform magnetic field

In a uniform magnetic field, all electrons have $\Delta_j = 0$. Eqs. (8) can be solved exactly in this regime by introducing the superradiant mode b_c that couples directly to the cavity and the $N-1$ subradiant modes orthogonal to it,

$$b_j = \eta_j b_c / \sqrt{N\langle|\eta|^2\rangle} + \text{orthogonal}, \tag{18a}$$

$$b_c = \sum_j \eta_j^* b_j / \sqrt{N\langle|\eta|^2\rangle}, \tag{18b}$$

where $\langle|\eta|^2\rangle = (1/N)\sum_j |\eta_j|^2$. (Two modes $\sum_j c_j b_j$ and $\sum_j c_j' b_j$ are orthogonal if $\sum_j c_j^* c_j' = 0$.) The orthogonal modes decouple from the system and decay with a rate γ, leaving only the superradiant mode coupled to the cavity,

$$i\dot{b}_0 = -\left(\Delta + i\frac{\Gamma}{2}\right) b_0 + \sqrt{N\langle|\eta^2|\rangle} b_c, \tag{19a}$$

$$i\dot{b}_c = -i\frac{\gamma}{2} b_c + \sqrt{N\langle|\eta|^2\rangle} b_0. \tag{19b}$$

These equations have the same form as (9) with $|\eta_1|^2$ replaced by $N\langle|\eta_1|^2\rangle$. Thus, for $N|\eta_1|^2 \ll \Gamma$ (equivalently $N\Gamma_1 \ll \Gamma$) the superradiant mode decays with a rate

$$\Gamma_N = N\Gamma_1 = \frac{4N\langle|\eta|^2\rangle}{\Gamma[1 + (2\Delta/\Gamma)^2]}. \tag{20}$$

This is a manifestation of Dicke superradiance,[25,26] since the superradiant mode contains on average $\sqrt{N}$ particles and has a radiation rate of $(\sqrt{N})^2 = N$ times that of a single particle.

The condition $N\Gamma_1 \ll \Gamma$ ensures the eigenmodes of the system are almost pure cavity or plasma modes. For later convenience we define the cavity-plasma mixing parameter

$$\chi_{\text{crit}} \equiv \omega^2/(NQ^2\eta) \sim \Gamma/(N\Gamma_1). \tag{21}$$

The cavity and plasma are largely unmixed for $\chi_{\text{crit}} \gg 1$ and mixing becomes strong as $\chi_{\text{crit}} \to 1$. In the strong mixing regime, we need the general form for the superradiant decay rate (obtained by solving for the eigenfrequencies of (19)):

$$\Gamma_N = \begin{cases} \frac{\Gamma}{2}\left(1 - \sqrt{1 - 16/\chi_{\text{crit}}}\right) & \text{for } \chi_{\text{crit}} > 16, \\ \frac{\Gamma}{2} & \text{for } \chi_{\text{crit}} \le 16, \end{cases} \tag{22}$$

where we have set $\Delta, \gamma = 0$ for simplicity. We see that strong mixing causes both the cavity and plasma decay rates to become $\Gamma/2$, an effective shift of the cavity Q due to the plasma.

The above result has important implications for cavity cooling of the cyclotron motion. If the magnetic field is too uniform and there is nothing to disturb the electron normal modes, then one mode with energy $\sim k_B T$ will lose energy very rapidly. However, the $N-1$ other modes will lose their energy very slowly. Since N is a large number, this ideal system does not significantly benefit from coupling to the cavity mode.

2. Dephasing due to magnetic field gradient

We now turn to the case where the magnetic field is nonuniform, so that different electrons have differing cyclotron frequencies with spread $\delta\Omega$ (17). The superradiant mode can now mix with the subradiant modes through dephasing due to the spread in cyclotron frequencies. We study this behavior and how it affects removal of energy from cyclotron motion through numerical simulations in Section IV. Here we lay the theoretical groundwork for understanding the results.

To prepare, we simplify Eqs. (8) further by setting all $\eta_j = \eta$, with η real (this occurs, for example, when the plasma is small compared to the variation in the shape of the cavity mode). We introduce dimensionless time $\tau \equiv \eta t$, dimensionless decay rates $\tilde{\Gamma} \equiv \Gamma/\eta$, $\tilde{\gamma} \equiv \gamma/\eta$, and dimensionless detunings $\tilde{\Delta} \equiv \Delta/\eta$, $\tilde{\Delta}_j \equiv \Delta_j/\eta$. Unless noted otherwise, a tilde on a quantity with units of frequency will indicate rescaling by η. In dimensionless variables, the basic coupling equations become

$$i\frac{\mathrm{d}b_0}{\mathrm{d}\tau} = -\left(\tilde{\Delta} + i\frac{\tilde{\Gamma}}{2}\right) b_0 + \sum_j b_j, \tag{23a}$$

$$i\frac{\mathrm{d}b_j}{\mathrm{d}\tau} = \left(\tilde{\Delta}_j - i\frac{\tilde{\gamma}}{2}\right) b_j + b_0. \tag{23b}$$

We set $\tilde{\Delta} = 0$, as its effect was discussed in Section III B. We will see that the decay of the energy in cyclotron motion is generally fast compared with the decay rate γ, so we set $\tilde{\gamma} = 0$ as this has little effect on our results. With these simplifications, Eqs. (23) are governed by three parameters: $\tilde{\Gamma}$, N, and $\delta\tilde{\Omega} \equiv \delta\Omega/\eta$, the characteristic spread of the $\tilde{\Delta}_j$. Typical experimental parameters considered in this paper are equivalent to normalized parameter values $\tilde{\Gamma} \sim 10^3 - 10^4$, $N \sim 10^3 - 10^7$, and $\delta\tilde{\Omega} \sim 0 - 2\tilde{\Gamma} \sim 0 - 10^4$. The dimensionless single electron decay rate satisfies (when $\tilde{\Delta} = 0$) $\tilde{\Gamma}_1 = 4/\tilde{\Gamma} \sim 10^{-4} - 10^{-3}$.

With the help of simulations (see Section IV) we identify several important regimes. When $N\tilde{\Gamma}_1 \ll \tilde{\Gamma}$ and detuning is small, $\delta\tilde{\Omega} \ll \tilde{\Gamma}$, the system in (23) can be thought of as a perturbation to the uniform magnetic field case discussed in Section III C 1. That is, the subradiant modes are weakly coupled to the superradiant mode – cavity mode system (19). In this small detuning regime, the rate at which energy is extracted from cyclotron motion is governed by the parameter

$$\chi \equiv (\delta\tilde{\Omega})\tilde{\Gamma}/N = (\delta\Omega)\omega/(NQ\eta^2) \sim \delta\Omega/(N\Gamma_1), \tag{24}$$

the ratio of average frequency spread to the single-particle decay rate. The transition from small to large detuning occurs as $\delta\tilde{\Omega} \to \tilde{\Gamma}$ or equivalently as $\chi \to \tilde{\Gamma}^2/N = \chi_{\mathrm{crit}}$. This critical χ, χ_{crit} was introduced in Eq. (21), where it was shown to govern the level of mixing between plasma and cavity.

We can now use χ and χ_{crit} in place of $\delta\tilde{\Omega}$ and $\tilde{\Gamma}$ to characterize the behavior of cyclotron cooling, and the above discussion indicates the existence of four regimes, defined by whether $\chi \ll \chi_{\mathrm{crit}}$ or not and whether $\chi_{\mathrm{crit}} \gg 16$ or not (see Eq. (22)). However, for small χ_{crit} (of order 16 or less), there is very little cavity-enhanced cooling of the plasma, no matter the value of χ. This effectively gives us a single regime, which we refer to as weak cooling. For large χ_{crit}, we have the small detuning ($\chi \ll \chi_{\mathrm{crit}}$) and large detuning ($\chi \gtrsim \chi_{\mathrm{crit}}$) regimes. Both of these regimes can support relatively strong cooling, with improved cooling at larger χ in the small detuning regime and smaller χ in the large detuning regime. See Fig. 1 for details on the small detuning regime and Fig. 2 for a graphical summary of the behavior in the different regimes.

One might wonder how particle number affects these regimes, but an interesting feature of (23) is that at fixed χ and χ_{crit}, the behavior of the system in normalized time $\tilde{\Gamma}\tau = \Gamma_1 t$ is largely independent of N. Specifically, the dimensionless decay rate (normalized to $\tilde{\Gamma}_1$) for $N \sim 1000$ particles differs from the decay rate at larger N (at fixed χ and χ_{crit}) by less than $\sim 1\%$. This is because the particle number N plays two roles. On the one hand, N sets the parameters of the system such as χ and χ_{Crit}; on the other hand, N sets the number of random draws from a continuum Vlasov-like distribution (see Appendix B for more details on this continuum limit). By disentangling these roles, we can simulate a plasma of N_e electrons using only $N_m \ll N_e$ macroparticles (random draws). Since the current is $\propto Nq$ and the coupling to the cavity has strength $\propto q/m$, we need to keep $N_m q_m^2/m_m = N_e e^2/m_e$ fixed to ensure the correct system parameters independent of the number of samples N_m. This corresponds to holding $N\eta^2$ fixed and thus also holding $\chi = (\delta\Omega)\Gamma/(N\eta^2)$ and $\chi_{\mathrm{crit}} = \Gamma^2/(N\eta^2)$ fixed. After setting χ and χ_{crit} using the true plasma and cavity parameters (using the true particle number N_e), the remaining N in our model is just the macroparticle number N_m, which we can set as low as $N_m \sim 1000$ to properly simulate the plasma.

IV. CAVITY INTERACTION WITH AXIALLY STATIONARY ELECTRONS: NUMERICAL SIMULATION AND ANALYSIS

A. Small Detuning, $\chi \ll \chi_{\mathrm{crit}}$, $\chi_{\mathrm{crit}} \gg 16$

We now solve Eqs. (23) numerically. We first look at the regime where the electron cyclotron frequencies are well within the linewidth of the cavity, $\delta\tilde{\Omega} \ll \tilde{\Gamma}$. The parameters for the simulations were chosen to match those for the TE_{121} mode of Ref. 6. The cavity frequency is $\omega = 2\pi \times 21.8$ GHz with a decay rate of $\Gamma = \omega/1580$. The effective mode volume is $V = (1/0.83)\ \mathrm{cm}^3$, which leads to a resonant single-electron decay rate of $\Gamma_1 = 4\eta^2/\Gamma = 60.9\ \mathrm{s}^{-1}$.

In all calculations, the amplitude of each electron's cyclotron motion, b_j, is chosen randomly with a Gaussian distri-

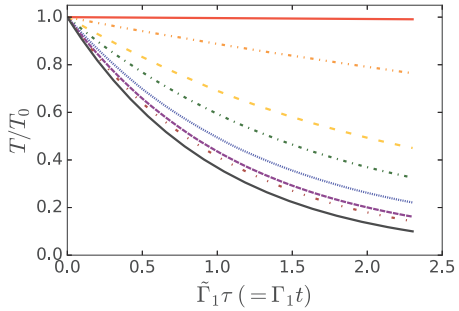

Figure 1. Evolution of the normalized temperature T/T_0 of $N = 1000$ electrons with respect to the dimensionless time parameter $\tilde{\Gamma}_1\tau$ is shown. The electrons are given random cyclotron frequencies drawn from a uniform distribution with standard deviation $\delta\Omega$. The top seven curves correspond to $\chi = 0, 1, 3, 5, 10, 20,$ and 30 with greater cooling at larger χ. The steepest decay corresponds to the single electron result with decay rate $\tilde{\Gamma}_1$. In this simulation the electrons are coupled to a TE_{121} cavity mode with $\chi_{\text{crit}} \approx 5700$.

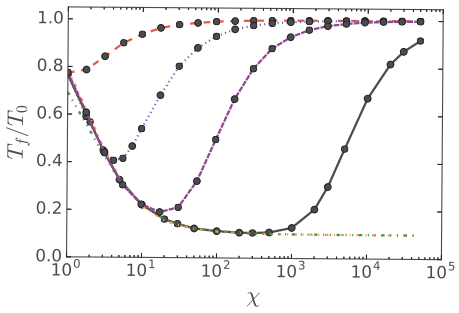

Figure 2. The dependence of the normalized final temperature T_f/T_0 on the frequency spread χ plotted for different cavity parameters χ_{crit}. We use the final time $t_f = \ln(10)/\Gamma_1$. The curves with simulated data marked by dots correspond to $\chi_{\text{crit}} = 1, 10, 100,$ and approximately 5700 with greater cooling at larger χ_{crit}. The final temperatures from Fig. 1 correspond to the left portion of the $\chi_{\text{crit}} \approx 5700$ curve. For comparison we display the solutions to the rate Eqs. (26) (the two curves with no markers). The dash-dot-dotted green and dashed-dotted orange curves correspond to $\tilde{\Gamma}_{bc} = 0.19\chi\tilde{\Gamma}_1$ and $\tilde{\Gamma}_{bc} = \tilde{\Gamma}_1\chi^2/(4+8\chi/\sqrt{3})$ respectively. The disagreement between simulations and the rate equations begins at $\chi \sim 0.1\chi_{\text{crit}}$ for large χ_{crit} and at $\chi \sim \chi_{\text{crit}}$ for small χ_{crit}. This indicates the onset of the large detuning regime.

bution for the real and imaginary parts so that the temperature starts at 1000 K. This will simulate an initial thermal distribution for the cyclotron motion. We are interested in how this temperature evolves with time for different $\chi = (\delta\tilde{\Omega})\tilde{\Gamma}/N$. Note that we require $N\chi \ll \tilde{\Gamma}^2 \sim 6\times10^6$ to stay in the small detuning regime considered in this section. At $N = 1000$ particles (the number used in our simulations), this corresponds to $\chi \ll 6000$. We use the average kinetic energy of the electrons $\langle K\rangle = (1/N)\sum_j m|v_{j-}|^2/2 \propto \sum_j |b_j|^2$ as a proxy for the electron temperature (ignoring that the distribution may become non-thermal during cooling). We solved (23) for 50 different (random) initial conditions so that 50,000 electrons were simulated.

The time dependence of the cyclotron temperature is shown in Fig. 1 for different values of χ. The decay rate increases as χ increases; the different curves correspond to $\chi = 0$, 1, 3, 5, 10, 20, and 30. For comparison, we also show the single-electron case, which is the fastest decay in the plot. The final time in the plot is such that the single electron decay loses 90% of its initial energy through coupling to the cavity ($\tau_f = \ln(10)/\tilde{\Gamma}_1$). The effect of $\tilde{\gamma}$ is negligible as $\tilde{\gamma}\tau_f \simeq 9\times10^{-3}$.

As expected from Section III C 1, the case when $\chi = 0 \Rightarrow \tilde{\Delta}_j = 0$ gives no appreciable decay when there are a large number of electrons in the plasma. With increasing spacing (χ), the decay rate increases because the subradiant modes will mix with the superradiant mode b_c as the individual amplitudes b_j accumulate a phase relative to each other. This increase in the decay rate is explicitly shown in Fig. 2, where the left portion of the solid black curve has the final temperatures from Fig. 1 plotted against χ. Note that as χ passes $0.1\chi_{\text{crit}} \simeq 570$, we leave the small detuning regime and the decay rate starts to decrease with increasing χ.

B. Adiabatic Approximation, $\chi \ll \chi_{\text{crit}}$, $\chi_{\text{crit}} \gg 16$

For the cooling of electrons, it is important to have an estimate of how fast energy is removed from the plasma for non-zero, but small, average spacing. In this section, we derive the decay of the cyclotron energy for this case, under the assumption that Δ, Γ are much larger than any other frequency in the system (η, Δ_j). In this regime, we can adiabatically eliminate the cavity mode from (8),

$$b_0 \simeq -\sum_j \frac{i\eta_j^*}{-i\Delta+\Gamma/2} b_j, \tag{25a}$$

$$i\dot{b}_j \simeq \left(\Delta_j - i\frac{\gamma}{2}\right) b_j + \sum_{j'} \frac{\eta_j\eta_{j'}^*}{\Delta+i\Gamma/2} b_{j'}. \tag{25b}$$

The adiabatic approximation helps with numerical calculations because numerically integrating the original Eqs. (23) requires time steps $\delta\tau \sim 1/\tilde{\Gamma}$ ($\delta t \sim 1/\Gamma$), whereas the approximate Eqs. (25) can use time steps $\delta\tau \sim 1/(N\tilde{\Gamma}_1)$ ($\delta t \sim 1/(N\Gamma_1)$) that are much larger, at least for $N < 10^6$. Eqs. (25) were numerically tested and worked well in the limit where $\eta_j\eta_{j'}^*/\Gamma$ was fixed and $\Gamma \to \infty$.

C. Rate Equations, $\chi \ll \chi_{\text{crit}}$, $\chi_{\text{crit}} \gg 16$

In this section, we explore the possibility for using rate equations to describe the coupling of the electrons' cyclotron motion to a cavity. These equations arise from thinking of

the system (23) as partitioned into three oscillators that are coupled together. The cavity is only coupled to the collective mode so that the energy is transferred with a rate $N\tilde{\Gamma}_1$. The other modes are coupled to the collective mode with a rate proportional to the dephasing $\chi = (\delta\tilde{\Omega})\tilde{\Gamma}/N$. This suggests the coupled equations (for $\tilde{\Delta}, \tilde{\gamma} = 0$)

$$\frac{dT_{cav}}{d\tau} = -\tilde{\Gamma}T_{cav} + N\tilde{\Gamma}_1(T_c - T_{cav}), \tag{26a}$$

$$\frac{dT_c}{d\tau} = -N\tilde{\Gamma}_1(T_c - T_{cav}) + (N-1)\tilde{\Gamma}_{bc}(T_b - T_c), \tag{26b}$$

$$\frac{dT_b}{d\tau} = -\tilde{\Gamma}_{bc}(T_b - T_c), \tag{26c}$$

where $\tilde{\Gamma}_{bc}$ is the rate for energy to be removed from the non-collective modes and put into the collective mode, $T_{cav} \sim |b_0|^2$ is the cavity temperature, $T_c \sim |b_c|^2$ is the temperature of the collective mode, $T_b \sim \sum_j |b_j|^2$ is the temperature of the $N-1$ non-collective modes, and we have assumed the cavity is coupled to a zero temperature bath. These equations correctly reproduce the $\chi \to 0$ limit (Eqs. (19)) and are an approximate generalization for finite χ. The final temperature of the electrons is $T_e = [(N-1)T_b + T_c]/N$. Because N is typically much larger than 1, we have $N-1 \approx N$ and $T_e \approx T_b$. The case we consider has $\tilde{\Gamma} \gg N\tilde{\Gamma}_1$, which means $T_{cav} \ll T_c$. Thus the cavity temperature decouples from (26), leaving $T_f/T_0 \simeq \exp(-\tilde{\Gamma}_e\tau_f)$ with $\tilde{\Gamma}_e \simeq \tilde{\Gamma}_{bc}\tilde{\Gamma}_1/(\tilde{\Gamma}_1 + \tilde{\Gamma}_{bc})$.

The simplest form for the coupling between the collective and non-collective modes is to take $\Gamma_{bc} \propto \delta\Omega/N$ ($\tilde{\Gamma}_{bc} \propto \chi\tilde{\Gamma}_1$). This produces the green dash-dot-dotted line in Fig. 2, which is best fit at large χ ($1 \ll \chi \ll \chi_{crit}$) when $\tilde{\Gamma}_{bc} = 0.19\chi\tilde{\Gamma}_1$. However, it is clear from Fig. 2 that this strongly overestimates the rate at small χ. We used a simple form for $\tilde{\Gamma}_{bc}$ which has the correct behavior for both small χ (based on (**??**)) and larger χ:

$$\tilde{\Gamma}_{bc} = \frac{12\delta\tilde{\Omega}^2/N^2}{3\tilde{\Gamma}_1 + 4\sqrt{12}\delta\tilde{\Omega}/N} = \frac{\chi^2}{1 + 2\chi/\sqrt{3}}(\tilde{\Gamma}_1/4). \tag{27}$$

As can be seen in Fig. 2 (orange dash-dotted line), this form gives good results for all $\chi \ll \chi_{crit}$, even though it is an ad hoc fit to the behavior at small and large χ. Since $\tilde{\Gamma}_e \propto \tilde{\Gamma}_1$, with the proportionality only a function of χ, and since $\tilde{\Gamma}_1\tau_f$ is fixed, the rate equation solution for T_f/T_0 will only depend on χ. This is a general feature of the system (23): for $\chi \ll \chi_{crit}$ the decay rate rescaled by Γ_1 depends only on χ (for $\tilde{\gamma}, \tilde{\Delta} \approx 0$).

These rate equations only hold when the total spread in frequency is much smaller than the cavity linewidth, Γ. For a total spread comparable to or larger than Γ, some of the electrons are outside of the linewidth of the cavity, requiring a modification to the rate equations.

D. Large Detuning and Weak Cooling Regimes, $\chi \gtrsim \chi_{crit}$

The case where there are many electrons coupled to a cavity mode was considered in Ref. 7. There the argument was made that the optimum spread of frequencies is $\delta\tilde{\Omega} \simeq \tilde{\Gamma}$. The basic idea is that the dephasing rate of the collective mode is proportional to $\delta\tilde{\Omega}$, and this is competing with the fact that the decay rate decreases when the cyclotron frequency is outside of the cavity linewidth. Since the single-electron decay rate is $\tilde{\Gamma}_1/[1 + (2\tilde{\Delta}/\tilde{\Gamma})^2]$, having $\tilde{\Delta} > \tilde{\Gamma}/2$ quickly decreases the single-electron decay rate suggesting the fastest decay should have $\delta\tilde{\Omega} \sim \tilde{\Gamma}$. We refine this discussion below.

The calculations based on (23) are the most relevant for this case because the cavity response cannot be treated as fast compared to the other time scales in the problem. Because $\delta\tilde{\Omega}$ is comparable to or larger than $\tilde{\Gamma}$, we will define $\tilde{\Gamma}_1$ to be the single-electron decay rate exactly on resonance; the decrease in the decay rate due to detuning will be explicitly shown when needed.

We now determine what frequency spread is optimal for maximizing the cooling rate. Fig. 2 shows the final temperature at a time when the single-electron case has decreased by a factor of 10 ($\tau_f = \ln(10)/\tilde{\Gamma}_1$). The different curves with markers are for $\chi_{crit} =$ 1, 10, 100, and $\simeq$ 5700, with better cooling at larger χ_{crit}. The markers are the results of simulations run for $N = 1000$ particles, averaged over 50 random initial conditions. Better cooling at larger χ_{crit} is natural since $\chi_{crit} \sim \tilde{\Gamma}^2$ and the faster the cavity mode decays, the more quickly we can remove energy from the plasma. For a large χ_{crit} ($\gg 16$), there is a wide range of χ available for optimal cooling. We need $\chi \gg 1$ to have good mixing into the collective mode, but this effect saturates at $\chi \sim 60$. From there, the cooling is essentially constant as a function of χ until we enter the large detuning regime at $\chi/\chi_{crit} = \delta\Omega/\Gamma \sim 0.1$. At this point, more and more electrons fall outside the linewidth of the cavity, resulting in worsening cooling with increasing spread χ. For smaller values of χ_{crit}, the large detuning regime begins before the mixing into the collective mode saturates. This increases the optimal frequency spread χ/χ_{crit}, but at the cost of less cooling at the optimum. From Fig. 2, we see that the optimal χ/χ_{crit} increases to about 0.2 for $\chi_{crit} = 100$, about 0.5 for $\chi_{crit} = 10$, and about 1 for $\chi_{crit} = 1$.

We may alternatively plot the final temperature as a function of χ_{crit} for different χ, as shown in Fig. 3. The different curves are for $\chi = 0.1$, 1, 5, and 30, with larger χ giving lower temperatures at large χ_{crit}. Since $\tilde{\Gamma}$ will typically be fixed by the cavity, we have $\chi_{crit} \propto 1/N$ and may regard Fig. 3 as a plot versus (inverse) particle number. At small particle number (large χ_{crit}) increasing the frequency spread improves cooling since all χ in the figure are much smaller than χ_{crit}. This is in accord with the results of Fig. 2. For large particle numbers (small χ_{crit}) we have the opposite effect: decreasing the frequency spread brings many electrons back into the linewidth of the cavity and improves cooling. We can understand why the curves in Fig. 3 cross and reverse their ordering by looking back at Fig. 2. The chosen values of $\chi = 0.1, 1, 5, 30$ will lie on the decreasing (left) portion of a χ_{crit} curve when $\chi_{crit} \gg 30$, so the lowest temperature will belong to the largest χ in this regime. Conversely, when $\chi_{crit} \lesssim 0.1$, the chosen χ will lie on the increasing (right) portion of a χ_{crit} curve and so the lowest temperature will belong to the smallest χ in this regime. Between these regimes, the lowest temperature will switch from the smallest to the largest χ, depending on how the χ distribute themselves around the minimum of a χ_{crit} curve.

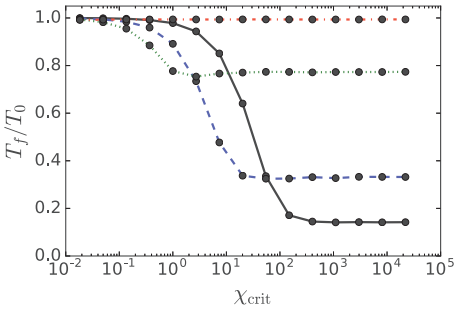

Figure 3. The dependence of the normalized temperature T_f/T_0 on $\chi_{\rm crit}$ for different values of χ is shown. The curves correspond to $\chi =$ 0.1 (red dash-dot), 1 (green dot), 5 (blue dash), and 30 (black solid). At low $\chi_{\rm crit}$ there is almost no cooling since most of the electrons are outside the linewidth of the cavity.

E. Discussion

Putting everything together, we see that plasma cooling is governed by a combination of single- and multi-electron effects. For optimal cooling, we need to maximize the (on-resonance) single-particle decay rate $\Gamma_1 = (2e^2/m_e\varepsilon_0)(|h|^2Q/V\omega)$, while allowing for a large detuning still within the cavity linewidth, $N\Gamma_1 \ll \delta\Omega \lesssim \omega/Q$. From the simulation results (see in particular Fig. 2), optimal cooling can be achieved by satisfying $10N\Gamma_1 \lesssim \delta\Omega \lesssim 0.1\Gamma$, and maximizing Γ_1 subject to these constraints. Typically, this results in equating $10N\Gamma_1 \sim \delta\Omega \sim 0.1\Gamma$, which places a strong constraint on the cavity Q-factor (for a given number of particles).

For more detailed analysis of the cooling dynamics, we make use of the dimensionless parameters $\chi = 4\delta\Omega/(N\Gamma_1)$ and $\chi_{\rm crit} = 4\omega/(QN\Gamma_1)$ together with the simulation results displayed in Fig. 2 and Fig. 3. For example, if we are interested in cooling 10^6 electrons in a cavity with Q-factor 1580 at a frequency of $\omega = 2\pi \times 21.8$ GHz using a cavity mode with effective volume $V = 1.2$ cm^3 and a magnetic field gradient of $\delta B \sim 10^{-3}$ T, we compute χ and $\chi_{\rm crit}$ for our setup:

$$\chi = \frac{4\delta\Omega}{N\Gamma_1} = \frac{2\delta B}{N}\frac{\varepsilon_0}{e}\frac{V\omega}{|h|^2Q} \sim 11.5, \tag{28a}$$

$$\chi_{\rm crit} = \frac{4\omega}{QN\Gamma_1} = \frac{2}{N}\frac{m\varepsilon_0}{e^2}\frac{V\omega^2}{|h|^2Q^2} \sim 5.7, \tag{28b}$$

where we have assumed our plasma is located near an antinode ($h \sim 1$). We can now look at Fig. 2 where $\chi \sim 11.5$ and $\chi_{\rm crit} \sim 5.7$ (between the red dashed curve and blue dotted curve). This shows our plasma will lose approximately 15% of its initial energy within $\Delta t = \ln(10)/\Gamma_1 \sim 38$ ms.

We can see from the graph that we are far from optimal cooling. We can decrease the magnetic field gradient, reducing χ by about a factor of two so that the plasma loses more than 30% of its energy in the same amount of time. Alternatively, we can decrease Q by a factor of four, increasing $\chi_{\rm crit}$ to about 90, letting the plasma lose about 75% of its energy in $\Delta t = 4 \times 38$ ms.

As another example, we compare our (axially stationary electron) model to experimental data in Fig. 4. The experiment cooled $N = 3 \times 10^7$ electrons located near the antinode of a TE_{111} cavity mode with $\omega = 5.1 \times 10^{10}\,s^{-1}$, $Q \sim 700$, and mode volume $V = 10^{-5}$m, as described in Ref. 12. Four different magnetic field gradients were applied to both short ($L = 36$ mm) and long ($L = 63$ mm) plasmas, resulting in eight different frequency spreads Δf (denoting the full-width frequency spread). This gives dimensionless parameters $\chi_{\rm crit} = 3.5$ and $\chi = (8.8 \times 10^{-2})\Delta f$ (MHz). The model curve is constructed from simulations using these parameters and a total of 5×10^4 macroparticles. The agreement between model and experiment is reasonable: peak cooling is predicted to within 10%-20% and the optimal frequency spread to within 50%. The significant disagreement at larger frequency spread results from the plasma coupling to nearby modes, producing enhanced cooling. We note that agreement between data and experiment gets worse at smaller particle number. There the plasma does not flatten the potential as much, making effects of axial motion more important. Better agreement can be obtained by accounting for axial motion, additional mode coupling, and uncertainties in experimental parameters (which can be as large as 30%), but the reasonable success of the simple model is already promising.

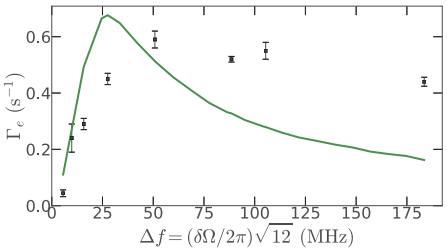

Figure 4. Comparison of experimental cooling rates (squares) with model predictions using axially-stationary electrons (solid green line). The black squares are data for short ($L = 36$mm) plasma and the white squares are data for long ($L = 63$mm) plasma. Both plasmas were subjected to the same four magnetic field gradients. Peak cooling rate and optimal frequency spread are predicted reasonably well. Disagreement at larger frequency spread is expected due to the plasma coupling to nearby modes and from effects of axial motion.

V. MOVING ELECTRONS COUPLED TO A CAVITY MODE

In this section we allow the centers of the electron cyclotron orbits to move. The centers follow a guiding center motion, oscillating axially with characteristic bounce frequencies $\omega_{b,j}$ (we ignore any electron-electron interactions,

including collisions). We characterize the distribution of bounce frequencies using the average $\bar{\omega}_b \equiv \sum_j \omega_{b,j}/N$ and RMS spread $\delta\omega_b$. This results in time-dependent cyclotron frequencies $\Omega_j(t) = e|\boldsymbol{B}_{\rm ext}(\boldsymbol{x}_j(t))|/m_e$ and cavity couplings $\eta_j(t) = eh_-(\boldsymbol{x}_j(t))/\sqrt{2m_eV\varepsilon_0}$, where $\boldsymbol{x}_j(t) = \boldsymbol{r}_{j\perp} + z_j(t)\hat{\boldsymbol{z}}$ and $\boldsymbol{r}_{j\perp}$ is the transverse position of the guiding center for electron j. The transverse position of the electron relative to its guiding center is absent from the above equations because the cyclotron radius is much smaller than the variation in $\boldsymbol{B}_{\rm ext}$ and h_-. The coefficients on the right-hand side of Eqs. (8) are thus time-dependent, and though we may still regard (8) as a Schrödinger equation $i\mathrm{d}|b\rangle/\mathrm{d}t = M(t)|b\rangle$, the formal solution is now the time-ordered exponential $|b(t)\rangle = \mathscr{T}\exp\left(-i\int M(t)\,\mathrm{d}t\right)|b(0)\rangle$. The formal solution is useful when treating the time-dependence as a perturbation to the time-independent system; however, for the cases of interest, the time-dependent contribution will often be large and cannot be handled perturbatively. Instead, we will numerically integrate (8) using the methods discussed in Appendix A.

We split our analysis of axial motion into two cases. In the first case, we examine the effect of the time-dependent cavity coupling $\eta_j(t)$ assuming the axial magnetic field is very nearly uniform so that (averaging over axial motion) $\Omega_j \approx \bar{\Omega} \to \Delta_j \approx 0$. This type of axial motion produces sidebands in the cooling rate (as a function of Δ), allowing the plasma to cool away from the central resonance. Since the only cooling is due to the time-dependence of η, axial motion leading to a strong oscillatory component of $\eta(t)$ improves the plasma cooling rate. In the second case, we consider the effect of time-dependent cyclotron frequencies assuming (as in Section IV) that the plasma is small compared to the variation in the shape of the cavity mode, so $\eta_j(t) = \eta$ is time-independent. Here the cooling is due to the spread in cyclotron frequencies and axial motion tends to average this spread away. Thus in this case, we want to reduce the effect of axial motion to improve the cooling of the plasma.

When reporting our results in this section, we plot only the cyclotron (transverse) temperature of the plasma. The figures thus represent the rate at which energy is removed from cyclotron motion. Since axial motion is not cooled through coupling to the cavity, the actual cooling rate is typically one third lower.

Some rough estimates will guide whether we should think of $\bar{\omega}_b$ as being large or small. At 1000 K, an electron has a speed of $\sim 2\times10^5$ m/s. Taking the plasma length to be 1 cm gives a frequency of $\bar{f}_b \sim 10$ MHz and $\bar{\omega}_b = 2\pi\bar{f}_b \sim 10^8$ s^{-1}. This is comparable to the Γ for several of the cavity modes in Ref. 6. Lower temperatures and longer plasmas would lead to $\bar{\omega}_b$ substantially smaller than Γ.

A. Time-dependent Cavity Coupling

In this section, we examine the time-dependence $\eta_j(t)$ caused by electron axial motion and the spatial variation of $h_-(\boldsymbol{x})$. We assume the external magnetic field is sufficiently uniform to take $\Delta_j = 0$. As long as the plasma is not too long (compared to the cavity mode function), we can Taylor expand $\eta(z) = eh_-(\rho\approx0,z)/\sqrt{2m_eV\varepsilon_0}$, choosing $z=0$ as the center of the plasma: $\eta(z) = \eta + \eta' z + \eta'' z^2/2$. In particular, $\eta_j(t) = \eta(z_j(t)) = \eta + \eta' z_j(t) + \eta'' z_j^2(t)/2$. We set $\gamma = 0$ to isolate the effect of the time-dependent coupling. This simplifies Eqs. (8) to

$$i\frac{\mathrm{d}b_0}{\mathrm{d}t} = \left(-\Delta - i\frac{\Gamma}{2}\right)b_0 + \sum_j \eta_j^*(t)b_j, \tag{29a}$$

$$i\frac{\mathrm{d}b_j}{\mathrm{d}t} = \eta_j(t)b_0. \tag{29b}$$

Note that when the plasma is centered on a node, $\eta(t) = \eta' z(t)$ and when it is centered on an antinode, $\eta(t) = \eta + \eta'' z^2(t)/2$. These different forms for η can have important consequences for cooling. For example, small axial oscillations around an antinode will have essentially no effect on cooling (since $\eta''\delta z^2 \ll \eta$), while small axial oscillations around a node will produce a small, but typically noticeable effect.

1. *Single electron*

To understand some of the general features of (29), it is worthwhile to examine the single-electron case in detail, reducing (29) to two equations as we did in going from (8) to (9). With only one electron, $\omega_{b,1} = \bar{\omega}_b \equiv \omega_b$, and the analysis is simplest when $\Gamma_1 \ll \omega_b \ll \Gamma$. In this case, the cavity responds much faster than the changes to the cyclotron motion, so the cavity can be adiabatically eliminated,

$$b_0 \simeq -\frac{i\eta^*(t)}{-i\Delta+\Gamma/2}b_1, \tag{30a}$$

$$\frac{\mathrm{d}b_1}{\mathrm{d}t} \simeq -\frac{|\eta(t)|^2}{-i\Delta+\Gamma/2}b_1, \tag{30b}$$

$$b_1(t) \simeq \exp\left(\int_0^t [-i\delta\omega(t') - \Gamma_1(t')/2]\,\mathrm{d}t'\right)b_1(0), \tag{30c}$$

where $\delta\omega$ and Γ_1 are given by (15) and (16) respectively, with $|\eta|^2$ replaced by $|\eta(t)|^2$. Thus, there is not a substantial change to the single-electron result in this limit, except for the substitution of the instantaneous coupling. If the decay rate $\Gamma_1(t)$ is small compared to ω_b, then the long time behavior is determined by the time average of $|\eta(t)|^2$ and the energy in the cyclotron motion decays with a rate equal to the time average of $\Gamma_1(t)$.

When ω_b is of the same order as Γ (or larger) the results depend in detail on the behavior of $\eta(t)$. Since $z(t) = \sum_k z_k\exp(ik\omega_b t)$, we can expand $\eta(t) = \eta(z(t))$ as a power series in $\exp(i\omega_b t)$,

$$\eta(t) = \sum_{k=-\infty}^{\infty}\eta^{(k)}e^{ik\omega_b t}. \tag{31}$$

The coefficients $\eta^{(k)}$ depend on the functional form of $z(t)$. For example, when $\eta = \eta + \eta' z(t) + (1/2)\eta'' z^2(t)$ and $z(t) = z_0\cos(\omega_z t + \phi)$, the coefficients are $\eta^{(0)} = \eta +$

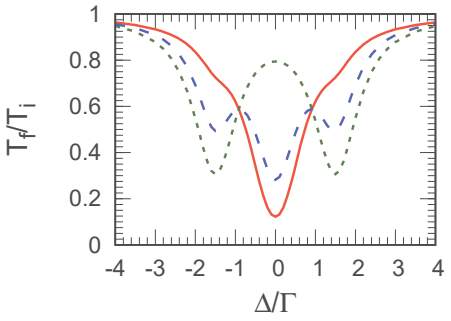

Figure 5. The ratio of final to initial cyclotron energy for the case of one electron with harmonic axial motion plotted versus the cavity detuning. The different curves all have an axial frequency $\omega_b = (3/2)\Gamma$, but with different amounts of oscillation in η. The final time is $\ln(10)/\Gamma_1(\beta = 0)$. The curves are for $\beta = \pi/10$ (solid red), $\pi/4$ (dashed blue), and $\pi/2$ (dotted green). The results of the single-electron equations are plotted but are indistinguishable from Eq. (37).

$\eta'' z_0^2/4$, $\eta^{(1)} = \eta^{(-1)*} = \eta' z_0 \exp(i\phi)/2$, and $\eta^{(2)} = \eta^{(-2)*} = \eta'' z_0^2 \exp(i2\phi)/8$.

Since the single-electron equations have the form $i|\dot{b}\rangle = M(t)|b\rangle$ with $M(t)$ periodic with frequency ω_b, we can perform a Floquet expansion for the b_0 and b_1. The two mode amplitudes can be written in terms of slowly evolving functions multiplied by oscillatory terms with angular frequency $k\omega_b$:

$$b_0(t) = \sum_{k=-\infty}^{\infty} b_0^{(k)}(t) e^{ik\omega_b t}, \tag{32a}$$

$$b_1(t) = \sum_{k=-\infty}^{\infty} b_1^{(k)}(t) e^{ik\omega_b t}, \tag{32b}$$

where the $b_\mu^{(k)}$ are slowly varying functions on the time scale of $\min(1/\omega_b, 1/\Gamma)$. Substituting (32) into the equation for b_0 and using the fact that we are interested in times $\Gamma t \gg 1$ gives

$$b_0^{(k)} \simeq \frac{1}{\Delta - k\omega_b + i\Gamma/2} \sum_\ell \eta^{(\ell)*} b_1^{(k-\ell)}. \tag{33}$$

Setting $b_1^{(k)}(t) = b_1^{(k)} \exp(-i\alpha t)$ and using the equation for b_1 gives an eigenvalue equation for the Floquet frequency α,

$$(\alpha - k\omega_z) b_1^{(k)} = \sum_\ell \eta^{(\ell)} b_0^{(k-\ell)}. \tag{34}$$

In general, α will need to be determined numerically. However, we can use a perturbative approach because we are interested in the case where $\eta \ll \Delta, \Gamma, \omega_b$.

The perturbative solution is constructed by starting with $b_1^{(0)} = 1$ and $\alpha = 0$. We represent the perturbative parameters η/Δ, η/Γ, and η/ω_b by the single quantity ε, because all three perturbative parameters are of the same order (typically much less than 10^{-3}). One can see that the other $b_1^{(k\neq 0)}$ are of order ε^2. Thus, to order ε^1,

$$b_0^{(k)} = \frac{\eta^{(k)*}}{\Delta - k\omega_b + i\Gamma/2} + \mathcal{O}(\varepsilon^3). \tag{35}$$

This result can be used in the $k = 0$ equation to obtain the solution for the Floquet frequency

$$\alpha = \sum_k \eta^{(k)} b_0^{(-k)} = \sum_{k\in\mathcal{N}_\eta} \frac{\eta^{(k)}\eta^{(-k)*}}{\Delta - k\omega_b + i\Gamma/2} + \mathcal{O}(\varepsilon^2), \tag{36}$$

where $\mathcal{N}_\eta \equiv \{k|\eta^{(k)} \neq 0\}$ counts the non-zero $\eta^{(k)}$. Since $\eta(t)$ is a real function, $\eta^{(-k)} = \eta^{(k)}$, so the single-electron decay rate $\Gamma_1 = -2\mathrm{Im}[\alpha]$ is

$$\Gamma_1 = \sum_{k\in\mathcal{N}_\eta} \frac{4|\eta^{(k)}|^2/\Gamma}{1 + [2(\Delta - k\omega_b)/\Gamma]^2}, \tag{37}$$

which shows Lorentzian sidebands at $\Delta = \pm k\omega_b$ with strengths proportional to the (square of the) appropriate Fourier component of the coupling.

Fig. 5 shows calculations for the case where the $\eta(t) = \eta[\cos\beta + \sqrt{2}\sin\beta\cos(\omega_b t)]$. This form of η was chosen so that the cycle average of η^2 was independent of the strength of the oscillatory component (as parameterized by β). This form for η has $\eta^{(0)} = \eta\cos\beta$ and $\eta^{(\pm 1)} = (1/\sqrt{2})\sin\beta$. We present calculations for three choices of β: a small oscillatory component in η ($\beta = \pi/10$), equal strength for the oscillatory and non-oscillatory components ($\beta = \pi/4$), and a purely oscillatory η ($\beta = \pi/2$). The plots show the ratio of the final to initial energy in the cyclotron motion as a function of the detuning for a final time $t_f = \ln(10)/\Gamma_1(\beta = 0)$ (when a non-oscillating electron has lost 90% of its energy). In all of the plots, $\omega_b = 3\Gamma/2$ and all of the other parameters are the same as in the earlier figures. The plots are from numerical solutions of the single-electron equations, but are indistinguishable from using $T_f/T_0 = \exp(-\Gamma_1 t)$ with Γ_1 given by (37).

2. *Many electrons*

The treatment is more subtle for many electrons, since now each electron can have a different $\omega_{b,j}$ and a different amplitude of oscillation. We first examine the case where $\omega_{b,j} \ll \Gamma$. The multi-electron generalization of (30a) and (30b) is

$$b_0 \simeq -\sum_j \frac{i\eta_j^*(t)}{-i\Delta + \Gamma/2} b_j, \tag{38a}$$

$$\frac{\mathrm{d}b_j}{\mathrm{d}t} \simeq -\sum_{j'} \frac{\eta_j(t)\eta_{j'}^*(t)}{-i\Delta + \Gamma/2} b_{j'}, \tag{38b}$$

which is the same as (25) except the η's are now time dependent. In the experimental cases we consider, $\bar{\omega}_b \gg \Gamma_1 \sim 4|\eta|^2/\Gamma$, so the time dependence of the η will be important.

The simplest case to treat is when $\omega_{b,j} = \bar{\omega}_b$ is the same for every electron. This occurs if the electrons are hot and in a

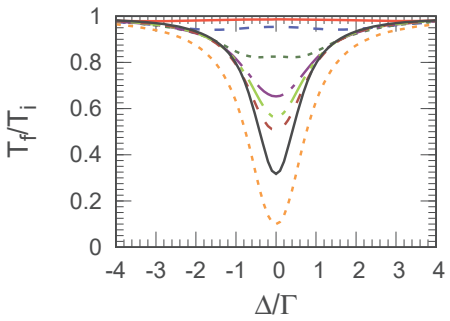

Figure 6. The ratio of final to initial cyclotron energy of $4^6 = 4096$ electrons (averaged over 4 runs) undergoing harmonic axial motion plotted versus cavity detuning. All curves have $\beta = \pi/4$, $\bar{\omega}_b = \widehat{\delta\omega}_b/2$, $N\Gamma_1/\Gamma = 0.2$, and a final time of $\ln(10)/\Gamma_1$. The different curves have an axial frequency spread $\widehat{\delta\omega}_b/(N\Gamma_1) = 0.1$ (solid red), 0.2 (medium-dash blue), 0.5 (short-dash green), 1.0 (long dash-dot purple), 1.5 (long dash-dot-dot light green) and 2.5 (medium-dash maroon). At $\Delta = 0$ the final temperature decreases with increasing $\widehat{\delta\omega}_b$. The single-electron result is the deepest short-dashed orange curve. The single-electron result dropping the $\eta^{(0)}$ term (i.e., the non-oscillating part of the coupling) is the deepest solid black line.

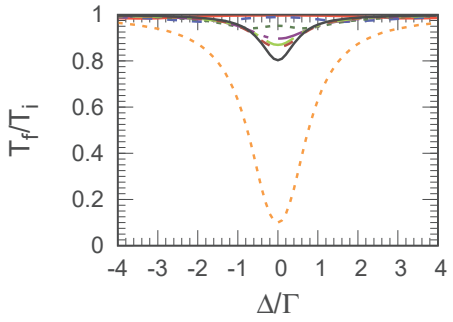

Figure 7. Same as Fig. 6 except $\beta = \pi/10$.

harmonic potential. Although all electrons have the same frequency, they will have different random phases to their axial motion. Since the rate that energy is removed from the plasma is $\propto \Gamma|b_0|^2$, it might be tempting to conclude from (38a) that the different phases will lead to an average of 0 for the cross terms and, thus, to enhanced cooling. However, this is incorrect because the b_j become correlated with η_j. This case is nearly as ineffective at removing energy from the plasma as the case where all the detunings are the same (see Section III C 1). One can see this by performing a cycle average

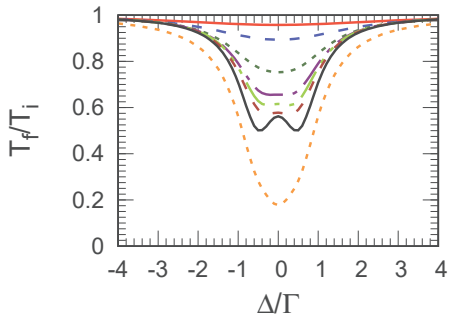

Figure 8. Same as Fig. 6 except $\bar{\omega}_b = \Gamma/2$.

on (38b), which gives

$$\frac{db_j}{dt} \simeq -\sum_{j'}\sum_{k\in\mathcal{N}_\eta} \frac{\eta_j^{(k)}\eta_{j'}^{(-k)*}}{-i\Delta+\Gamma/2} b_{j'}, \tag{39}$$

where $\mathcal{N}_\eta = \{k|\eta^{(k)} \neq 0\}$. The matrix on the right hand side of this equation is rank $|\mathcal{N}_\eta| = 2n_\eta + 1$, where n_η is the number of non-zero $\eta^{(k>0)}$. Thus, there will be $2n_\eta + 1$ modes that strongly decay and the rest, $N - (2n_\eta + 1) \simeq N$, will not decay at all. This observation is true whether or not each electron has a random phase or a random amplitude of oscillation.

There are three conditions that must hold for there to be substantial decay of the energy in the plasma. The first is that the oscillating part of η must be substantial; these are the $\eta^{(k\neq 0)}$. The second is that there needs to be a spread in the axial frequency of oscillation $\delta\omega_b$ that is larger than the decay rate of the collective mode, $N\Gamma_1$ (this corresponds to large axial χ). Finally, the spread in axial frequencies should be smaller than or comparable to Γ, otherwise there will be electrons outside the linewidth of the cavity. As with the case of stationary electrons, the last two conditions become impossible to simultaneously satisfy when $N\Gamma_1 > \Gamma$.

In the calculations that follow, every electron (in a particular run) has the same β but different phases and axial frequencies: $\eta_j(t) = \eta[\cos\beta + \sqrt{2}\sin\beta\cos(\omega_{b,j}t + \phi_j)]$. The phases are chosen from a uniform distribution between 0 and 2π. The frequencies are chosen from a uniform distribution centered on $\bar{\omega}_b$ with RMS spread $\delta\omega_b$. To simplify notation, we let $\widehat{\delta\omega}_b = \sqrt{12}\delta\omega_b$ be the full spread of the frequency distribution. We require $\bar{\omega}_b \geq \widehat{\delta\omega}_b/2$. We draw the cyclotron amplitudes from a thermal distribution as before. The final time was chosen so that one non-oscillating electron, perfectly on resonance with the cavity, loses 90% of its energy: $t_f = \ln(10)/\Gamma_1$. The calculations were performed varying N, Γ_1, β, $\bar{\omega}_b$, and $\delta\omega_b$. The calculations used $4^6 = 4096$ electrons per run and were averaged over 4 runs.

Figs. 6 ($\beta = \pi/4$) and 7 ($\beta = \pi/10$) show the final temperature for different $\bar{\omega}_b$ with $\bar{\omega}_b = \widehat{\delta\omega}_b/2$. As in Section IV,

we found that calculations with nearly the same scaled couplings and frequencies gave nearly identical results. For example, runs with fewer (e.g. $N = 4^5$) electrons gave nearly identical plots (not shown) when the rates and frequencies were appropriately scaled. These figures show two important trends. The first is that the energy can only be efficiently removed from the cyclotron motion when the spread in axial frequencies becomes comparable to or larger than $N\Gamma_1$. As with the results from the stationary electrons, we want $\chi_{\text{axial}} \equiv \delta\omega_b/(N\Gamma_1) \gg 1$. The second important trend is that the decay only comes from the oscillating term of the coupling. We can see this by comparing Fig. 6 to Fig. 7 as the only difference between them is the decrease in the amount of oscillation. Since the part of the decay rate depending on oscillation is proportional to $\sin^2\beta$, there is approximately a factor of 5 decrease in the decay rate between the figures. The importance of the oscillating component is particularly clear in Fig. 7 where the decay rates converge to the single-electron rate, where the latter is obtained using only the oscillating part of η.

Fig. 8 uses the same set of frequency spreads $\delta\omega_b$ as Fig. 6 but with the much larger $\bar{\omega}_b = \Gamma/2$. Comparison of these two figures shows that for smaller $\delta\omega_b$, the large $\bar{\omega}_b = \Gamma/2$ leads to more effective cooling than $\bar{\omega}_b \sim 0$. Based on the single-electron results, we would expect the opposite effect: for $\bar{\omega}_b \sim 0$, the Lorentzian sidebands at $\pm\bar{\omega}_b$ combine with the central resonant peak and enhance cooling, while for $\bar{\omega}_b = \Gamma/2$, the side bands stay separated. This phenomenon (better cooling at large $\bar{\omega}_b$) occurs because the non-oscillating part of η is contributing to Γ_1, so $\delta\omega_b/\Gamma_1$ is proportionally smaller (the decay is more blocked) when $\bar{\omega}_b \sim 0$. Once $\delta\omega_b$ is comparable to or larger than $N\Gamma_1$, the best decay rate is for $\bar{\omega}_b \sim 0$, in agreement with previous results since the decay in this limit approaches the single electron result.

The last case we consider is when the plasma is centered at an antinode of the cavity mode. We assume the plasma is sufficiently short compared to the spatial variation in the cavity mode so that we may use a second-order expansion $\eta(t) = \eta + (1/2)\eta'' z^2(t)$. When centered at an antinode, the coupling decreases away from $z = 0$, which means $\eta'' < 0$. The case where the axial motion is essentially harmonic does not introduce qualitatively new features. Writing the axial position as $z(t) = z_0\cos(\bar{\omega}_b t + \phi)$ gives a time dependence $\eta(t) = (\eta + \eta'' z_0^2/4) + (\eta'' z_0^2/4)\cos(2\bar{\omega}_b t + 2\phi)$. This is the same form as above but the frequencies and their spread are doubled. From the discussions above, only the oscillating term will lead to substantial cooling when there are many electrons. On resonance the maximum cooling rate will be half of the coefficient of the oscillating term: $\sim (1/2)4(\eta'' z_0^2/4)^2/\Gamma$.

Typically, the amplitude of the axial oscillation is such that the change in coupling is not very large (10-20%) because the size of the oscillating term is quadratic in the plasma length (as opposed to linear when the electrons are near a node). This strongly reduces the amount of coupling that is oscillating with time. Since the decay rate is proportional to the square of the oscillating component of η, time-dependent coupling due to axial motion will have little effect on cooling a plasma near an antinode, unless the plasma is long enough for $\eta(z)$ to vary substantially.

B. Time-dependent Frequency Shift

We now explore the effect of time-dependent cyclotron frequencies $\Omega_j(t)$ arising from electrons moving through an inhomogeneous magnetic field. We assume each electron's cyclotron frequency changes linearly with the distance from the center of the plasma, $\Omega_j(t) = \bar{\Omega} + \bar{\Omega}' z_j(t)$. As above, $z_j(t)$ is a periodic function, not necessarily a simple harmonic, with period $2\pi/\omega_{b,j}$. The coupling η between the cyclotron motion and the cavity will be taken to be a constant in this section. We again take $\gamma = 0$ for simplicity.

In this regime, Eqs. (8) become

$$i\frac{\mathrm{d}b_0}{\mathrm{d}t} = \left(-\Delta - i\frac{\Gamma}{2}\right)b_0 + \eta^*\sum_j b_j, \tag{40a}$$

$$i\frac{\mathrm{d}b_j}{\mathrm{d}t} = \Delta_j(t)b_j + \eta b_0, \tag{40b}$$

where $\Delta_j(t) = \bar{\Omega}' z_j(t)$. For the plasmas we consider, all of the electrons oscillate around the same z, which means that the cycle average of the detuning is approximately the same for every electron. Thus, we will only consider the case where the cycle average of Δ_j is zero; the average shift is in the parameter Δ. All of the results in this section were obtained by numerically solving (40). The approximations introduced below are mainly for the purpose of understanding the results.

1. Single electron

To understand some of the general features, it is worthwhile to examine the single-electron case in detail, reducing (40) to two equations as we did in going from (8) to (9).

We treat only the simplest case, where the time dependence in $\Delta_1(t)$ has frequencies much smaller than Γ and Δ. In this situation, the cavity oscillation can be adiabatically eliminated (see for example (25) and (30)),

$$\frac{\mathrm{d}b_1}{\mathrm{d}t} \simeq -\frac{|\eta|^2}{-i\Delta - i\Delta_1(t) + \Gamma/2}b_1, \tag{41a}$$

$$b_1(t) \simeq \exp\left(-\int_0^t [i\delta\omega(t') + \Gamma_1(t')/2]\,\mathrm{d}t'\right)b_1(0), \tag{41b}$$

where $\delta\omega$ and Γ_1 are given by (15) and (16) respectively, with Δ replaced by $\Delta + \Delta_1(t)$. Thus, the amplitude of oscillation is an exponential of a simple quadrature of the time-dependent frequency shift and decay rate.

Eq. (41b) exhibits an interesting feature when ω_b is much larger than Γ_1 (so there is very little decay during one period $2\pi/\omega_b$). On the time scale of the decay of the cyclotron motion,

$$\int_0^t \left[i\delta\omega(t') + \frac{\Gamma_1(t')}{2}\right]dt' \simeq i\langle\delta\omega\rangle t + \frac{\langle\Gamma_1\rangle}{2}t, \tag{42}$$

where the $\langle\rangle$ indicates an average over the period $2\pi/\omega_b$. Since $\langle\Delta_1\rangle = 0$, we have effectively the same situation as a stationary electron ($\Delta_1(t) = 0$) up to a relative error $\sim \langle\Delta_1^2\rangle/\Gamma^2$.

2. Many electrons

As with the case where the coupling was time dependent, the many-electron case has more subtlety because there is both an average bounce frequency $\bar{\omega}_b$ and a spread $\delta\omega_b$. We first examine the case where $\omega_{b,j}, \Delta_j, \eta_j \ll \Gamma, \Delta$. The multi-electron generalization of (41) is

$$b_0 \simeq -\frac{i\eta^*}{-i\Delta+\Gamma/2}\sum_j b_j, \tag{43a}$$

$$\frac{db_j}{dt} \simeq -i\Delta_j(t)b_j - \frac{|\eta|^2}{-i\Delta+\Gamma/2}\sum_{j'} b_{j'}, \tag{43b}$$

which is the same as (25) except the Δ_j's are now time dependent and $\eta_j = \eta$.

In the following calculations, the Δ_j will have a time dependence given by an approximate triangle function (with rounded corners) with period $2\pi/\omega_{b,j}$. The frequencies $\omega_{b,j}$ are chosen from a Gaussian distribution (with RMS spread $\delta\omega_b$), while the phase of $\Delta_j(t)$ is chosen from a uniform distribution. This approximately leads to a uniform distribution of detunings.

An extreme case is when the only difference in the $\Delta_j(t)$ is the phase: $\Delta_j(t) = \Delta_1(t - T_j)$. When the frequency $\bar{\omega}_b$ is larger than Γ_1, the decay is suppressed compared to the case where the Δ_j are time-independent. Since typically $\bar{\omega}_b > \Gamma_1$, we can expect that electrons oscillating identically but with different phases will not lead to strong coupling to the cavity. As with the time-dependent cavity coupling (Section V A), a spread in axial frequencies couples the plasma more strongly to the cavity.

Fig. 9 shows the final temperature as a function of the spread of detunings $\zeta = \sqrt{3}\chi/2$ for different $\delta\omega_b$. For all calculations, $N\Gamma_1 = \Gamma/20$ ($\chi_{\rm crit} = 80$) so that all of the electrons have frequencies within the linewidth of the cavity mode. We simulated $4^4 = 512$ electrons averaged over 16 different random configurations. The different lines correspond to $\widehat{\delta\omega}_b/\Gamma = 0$, 0.01, 0.02, 0.05, 0.1, 0.2, 0.5. The important point is the cooling rate is similar to that for stationary electrons when $\delta\omega_b \ll N\Gamma_1$. As the spread in axial frequencies becomes larger, energy is removed more slowly from the plasma. As long as the cavity cooling rate Γ is much larger than any other rate or frequency parameters, the plasma cooling rate is determined by the ratio $\chi_{\rm axial} = \delta\omega_b/(N\Gamma_1)$. For example, T_f/T_0 for $N\Gamma_1/\Gamma = 0.1$ and spread $\widehat{\delta\omega}_b/\Gamma = 0.2$ was nearly the same as for $N\Gamma_1/\Gamma = 0.05$ and spread $\widehat{\delta\omega}_b/\Gamma = 0.1$.

There is a small but interesting feature in Fig. 9. At larger values of ζ, the T_f for slowly moving electrons ($\widehat{\delta\omega}_b/\Gamma =$ 0.01 or 0.02) is somewhat lower than for stationary electrons. This effect is consistently present in the simulations, and we believe this is because the moving electrons have detuning distributions that fluctuate with time, giving a small additional mechanism for dephasing the cyclotron motion, leading to better mixing with the superradiant mode, and ultimately resulting in better cooling.

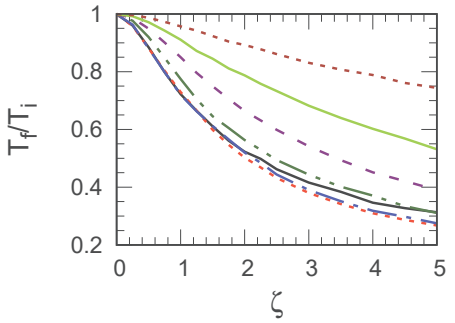

Figure 9. Ratio of final to initial cyclotron energy versus normalized frequency spread ζ for the case where the detuning oscillates. We may compare this with the results of non-oscillating detunings displayed in Fig. 2. All curves have $\chi_{\rm crit} = 80$. The different lines correspond to different axial frequency spreads $\chi_{\rm axial} = 0$ (solid black), 0.2 (short-dash red), 0.4 (dot-dash blue), 1 (dash-dot-dot green), 2 (medium-dash purple), 4 (solid light green), and 10 (short-dash maroon).

VI. COLLISIONS

Electron-electron collisions can affect cooling if they scatter energy into the collective mode. If the plasma is much smaller than the variation in the cavity mode shape, then electron-electron collisions have no effect on the collective mode and do not contribute to cooling. This is because the collective mode $b_c = \sum_j \eta_j b_j/\sqrt{N} = (\sum_j b_j)\eta/\sqrt{N}$ reduces to the center-of-mass mode, which cannot be affected by collisions. If the cavity mode varies along the plasma, then it may be possible for collisions to scatter into the collective mode, particularly for collisions whose scale is comparable to the variation of the cavity mode. Such collisions can occur (even for slowly-varying cavity modes) near the edge of the plasma, where Debye shielding produces large electric field gradients. Electron-electron collisions may thus provide another mechanism for dephasing the collective mode.

In this section we analyze a different type of collision: electrons colliding with background neutral atoms or molecules. There are two types of electron-neutral collisions to consider. The first type is inelastic scattering. At low electron energies, this will mainly result in momentum transfer between the neutral and the electron without any internal change of the neutral. This is a slow process due to the tiny electron to neutral mass ratio, so we ignore its effect on cooling here. The second type is nearly elastic scattering where only the direction of the electron's velocity changes. For now, we ignore any coupling

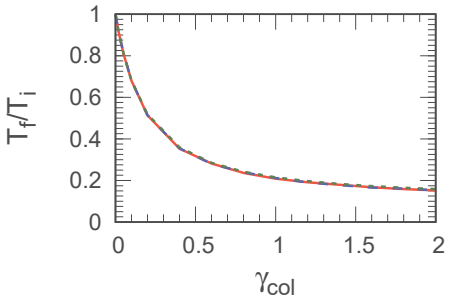

Figure 10. We use the same cavity parameters as in previous figures ($\Gamma = 8.67\times10^7 s^{-1}, \Gamma_1 = 60.9 s^{-1}$) and look at the effect of only collisions ($\chi = 0$). The two lines correspond to $4^5 = 1024$ (solid red) and to $4^6 = 4096$ (medium-dash blue) electrons. The final temperature is plotted versus the collision rate scaled by the superradiant rate: $\gamma_{col} = \Gamma_{col}/(N\Gamma_1)$. The third line plotted (short dash green) is the function $\exp(-\ln[10]\gamma_{col}/[0.5+\gamma_{col}])$. The lines are nearly indistinguishable.

such a collision might produce between the cyclotron and axial motion of the electron. Instead, we model the effect as an instantaneous change in the phase of b_j (when the jth electron collides with a neutral). This abrupt change in phase provides an additional mechanism for dephasing the collective mode, allowing energy to flow into it from the orthogonal modes.

For now, we fix the centers of the cyclotron orbits so that there is no axial motion. In particular, any scattering from background neutrals will only be in the transverse (non-axial) directions.

A. Collisions only

To isolate the effect of collisions, we consider (25) for the case where $\eta_j = \eta$ and $\Delta_j = \gamma = 0$. Without collisions, the cavity quickly removes the energy from the superradiant (collective) mode with a rate $N\Gamma_1$, but cannot remove energy from any of the subradiant (orthogonal) modes. To model collisions, we added a stochastic step to the equations. After every time step, δt, we cycled through each electron and compared a random number to a scattering probability $\Gamma_{col}\delta t$. If the random number is less than the scattering probability, then the b_j is multiplied by $\exp(i\phi)$ where ϕ is a random number between $-\pi$ and π. Perhaps surprisingly, within this model the rate that energy is lost through the cavity again depends only on parameters relative to $N\Gamma_1$.

Fig. 10 shows the results of including collisions for two different particle numbers $N = 4^5$ and 4^6 (with appropriately rescaled collision rate). As is clear from the figure, the final temperature at $t_f = \ln[10]/\Gamma_1$ only depends on the collision rate in units of the superradiant rate, as we again see the familiar invariance with respect to particle number. This simple model leads to a rate of energy loss approximately equal to $\Gamma_1\gamma_{col}/[0.5+\gamma_{col}])$, where $\gamma_{col} = \Gamma_{col}/(N\Gamma_1)$ is the scaled collision rate. Thus, the single-electron elastic scattering rate needs to be roughly equal to or larger than the superradiant rate for collisions to be important.

The scaling can be understood from a simple rate equation. As in section IV C, T_b is the temperature of the $N-1$ subradiant modes, and T_c is the temperature of the superradiant mode. The rate that collisions scatter energy from the subradiant modes into the superradiant one is proportional to the average energy in a subradiant mode k_bT_b times the single-electron collision rate. Similarly, the rate energy scatters out of the superradiant mode into the subradiant modes is proportional to the energy in the superradiant mode k_BT_c times the single-electron collision rate. For simplicity, take the proportionality constant to be $\mathscr{C}$. The rate equations for the energy flow are then

$$\frac{dT_c}{dt} = \mathscr{C}\Gamma_{col}(T_b - T_c) - N\Gamma_1 T_c, \tag{44a}$$

$$\frac{dT_b}{dt} = -\mathscr{C}\frac{\Gamma_{col}}{N}(T_b - T_c). \tag{44b}$$

The fastest possible decay is on a time scale of $\sim 1/\Gamma_1$ which is long compared to the inverse of the rates in (44a). Therefore, the time derivative of T_c must be small, leading to

$$T_c \simeq \frac{\mathscr{C}\Gamma_{col}}{\mathscr{C}\Gamma_{col} + N\Gamma_1}T_b. \tag{45}$$

Substituting this into the second equation gives

$$\frac{dT_b}{dt} = -\mathscr{C}\frac{\Gamma_{col}}{N}\frac{N\Gamma_1}{\mathscr{C}\Gamma_{col}+N\Gamma_1}T_b = -\Gamma_1\frac{\mathscr{C}\gamma_{col}}{\mathscr{C}\gamma_{col}+1}T_b, \tag{46}$$

where the scaled collision rate γ_{col} was defined above. We find $\mathscr{C} = 2$ from the fit line in Fig. 10.

B. Collisions plus a frequency spread

We now include the effects of both collisions and cyclotron frequency spread. We consider the case $\delta\Omega, N\Gamma_1, \Gamma_{col} \ll \Gamma$. We again set $\Delta = \gamma = 0$ and solve (30) using random phase jumps to model collisions. The rate Eqs. (26) and (44) generalize to

$$\frac{dT_{cav}}{dt} = -\Gamma T_{cav} + N\Gamma_1(T_c - T_{cav}), \tag{47a}$$

$$\frac{dT_c}{dt} = -N\Gamma_1(T_c - T_{cav}) + (N\Gamma_{bc} + 2\Gamma_{col})(T_b - T_c), \tag{47b}$$

$$\frac{dT_b}{dt} = -(\Gamma_{bc} + 2\Gamma_{col}/N)(T_b - T_c), \tag{47c}$$

where Γ_{bc} is from (27), Γ_{col} was discussed in Section VI A, T_c is the temperature of the collective mode, and T_b is the temperature of the $N-1$ non-collective modes. We have also taken $N \gg 1$ and coupled the cavity to a zero-temperature bath. The electron temperature is $T_e \approx T_b$. In Fig. 11 we mark the simulation results (solutions to (25), including the effects of collisions) as a function of frequency spread ζ for four different

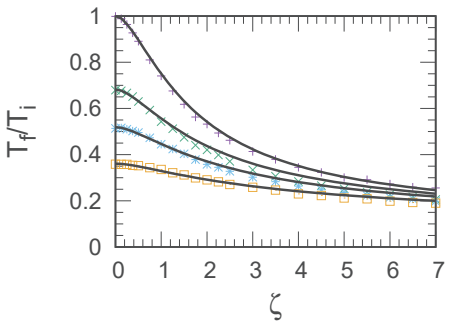

Figure 11. We plot the ratio of final to initial cyclotron energy versus normalized frequency spread ζ, including the effects of elastic collisions. We may compare this with results that ignore collisions, presented in Fig. 2. We illustrate results of four different scaled collision rates $\gamma_{\rm col} = \Gamma_{\rm col}/(N\Gamma_1)$, with markers for $\gamma_{\rm col} = 0$ (purple +), $\gamma_{\rm col} = 0.1$ (green X), $\gamma_{\rm col} = 0.2$ (blue *), and $\gamma_{\rm col} = 0.4$ (orange square). The lines are from the rate equation model (47).

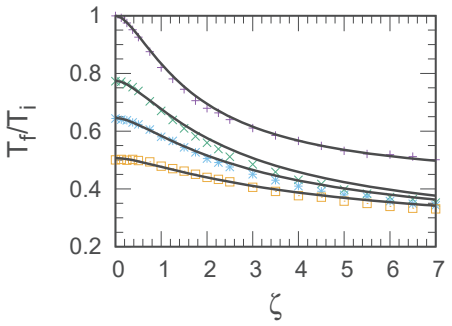

Figure 12. The same as Fig. 11 but for the case where elastic collisions mix in the axial motion. The final temperature (including T_z) is plotted versus the scaled spread in cyclotron frequency ζ for four different scaled collision rates $\gamma_{\rm col} = \Gamma_{\rm col}/(N\Gamma_1) = 0$ (purple +), 0.1 (green X), 0.2 (blue *), and 0.4 (orange square). The lines are from the rate equation model (48).

collision rates $\gamma_{\rm col}$. We plot the corresponding solutions to the rate Eqs. (47) as smooth lines. We see that the rate equations approximate the cases of pure collisions ($\zeta = 0$) and no collisions ($\gamma_{\rm col} = 0$) very well, but slightly underestimate the cooling rate for $\gamma_{\rm col} \sim 0.1$ and $\zeta > 3$.

C. Collisions plus axial motion

We now consider the more realistic scenario of collisions scattering electrons in three dimensions. We define a scaled axial velocity $b_{j,z}$ for each electron, following the definition of the transverse velocities b_j. When a collision occurs in the stochastic step, we fix the magnitude of the scaled velocity $b = (|b_\nu|^2 + b_{\nu,z}^2)^{1/2}$ and randomly rotate its direction with $\cos(\theta)$ chosen from a flat distribution between -1 and 1 and ϕ chosen from a flat distribution from 0 to 2π. The parameters after the collision are $b_j = b\sin(\theta)\exp(i\phi)$ and $b_{j,z} = b\cos(\theta)$. This model gave qualitatively similar results to the 2-dimensional model. The main difference is the rate of energy decrease is somewhat slowed because of the energy now being tracked in the axial motion.

The rate equations are modeled analogous to (47) with an extra temperature for the axial motion, T_z. The model we consider only has one quadratic degree of freedom for the axial motion so the electron temperature is $T_e = (2T_b + T_z)/3$. This means the change in temperature for the axial motion is twice that for the cyclotron motion. The equations generalize to

$$\frac{dT_{\rm cav}}{dt} = -\Gamma T_{\rm cav} + N\Gamma_1(T_c - T_{\rm cav}), \tag{48a}$$

$$\frac{dT_c}{dt} = -N\Gamma_1(T_c - T_{\rm cav}) + (N\Gamma_{bc} + 2\Gamma_{\rm col})(T_b - T_c), \tag{48b}$$

$$\frac{dT_b}{dt} = -(\Gamma_{bc} + 2\Gamma_{\rm col}/N)(T_b - T_c) - \Gamma_{\rm col}(T_b - T_z), \tag{48c}$$

$$\frac{dT_z}{dt} = 2\Gamma_{\rm col}(T_b - T_z). \tag{48d}$$

To account for a different number of degrees of freedom in the axial motion, one can change the factor multiplying $(T_b - T_z)$. The results of the model and rate equations are shown in Fig. 12 for $\Gamma \gg N\Gamma_1$. As with the collisions that did not account for the axial motion, the rate equations do an excellent job of reproducing the model but somewhat underestimate the rate for $\zeta > 3$ for a scaled collision rate $\gamma_{\rm col} \sim 0.1$.

VII. CONCLUSIONS

We presented a simple oscillator-based model describing cooling of a magnetized plasma that is nearly resonant with a microwave cavity mode. Our model reproduces the Purcell effect for a single electron, showing an enhanced decay rate inside a cavity. The behavior of the full plasma is governed by ratios of frequency spreads, the enhanced single-electron rate, and the cavity linewidth. Optimal cooling can be achieved by setting these roughly equal.

We identified several dimensionless parameters that helped categorize the different regimes of cooling (small detuning, large detuning, weak cooling). Cooling increases with frequency spread in the small detuning regime (since having too many electrons exactly resonant with the cavity mode is disadvantageous due to a collective mode blocking the decay) and decreases with frequency in the large detuning regime (as too many electrons leave the cavity linewidth). We showed how simple rate equations can describe the small detuning regime. We also identified a continuum limit, allowing for plasma simulations with many fewer macroparticles.

We showed how axial motion can either enhance cooling (by creating a spread in cavity mode coupling strengths) or

hinder cooling (by washing out the spread in cyclotron frequencies). Axial motion also provides sidebands, which allow the plasma to cool away from resonance. Collisions with background neutrals provide an additional source of dephasing, thus enhancing the cooling (at least in the small detuning regime).

Our model thus lays out a foundation for the theoretical understanding of magnetized plasma cooling inside a microwave cavity.

ACKNOWLEDGMENTS

This work was supported by the DOE OFES and NSF-DOE Program in Basic Plasma Science (USA) and NSERC (Canada).

DATA AVAILABILITY STATEMENT

Data sharing is not applicable to this article as no new data were created or analyzed in this study.

Appendix A: Numerical solution

Eqs. (8) can be solved using the Crank-Nicolson method or one that uses a higher order Padé approximation (order 2, for example) in the numerator and denominator. We start with (8) in the form

$$\frac{\mathrm{d}\vec{b}}{\mathrm{d}t} = -i\mathbf{M}(t)\vec{b}, \tag{A1}$$

where $-i\mathbf{M}$ is the matrix right hand side of (8).

If $\mathbf{M}$ is time-independent, then $\vec{b}(t) = \exp(-i\mathbf{M}t)\vec{b}(0)$. If $\boldsymbol{M}$ is time-dependent, we can use a sequence of small time steps $\vec{b}(t+\delta t) = \exp(-i\boldsymbol{M}(t+\delta t/2)\,\delta t)\vec{b}(t)$ to construct the solution. The Crank-Nicolson method is the lowest order Padé approximation of order 1 in the numerator and denominator,

$$e^{-i\mathbf{Q}} = \frac{1-i\mathbf{Q}/2}{1+i\mathbf{Q}/2} + O(\mathbf{Q}^3), \tag{A2}$$

with the error term being $i\mathbf{Q}^3/12$. This approximation works best when $\mathbf{M}$ is time-dependent. When $\mathbf{M}$ is time-independent, we use the Padé approximation of order 2 in the numerator and denominator,

$$\begin{aligned} e^{-i\mathbf{Q}} &= \frac{1-i\mathbf{Q}/2-\mathbf{Q}^2/12}{1+i\mathbf{Q}/2-\mathbf{Q}^2/12} + O(Q^5) \\ &= \left[\frac{1-ia\mathbf{Q}/2}{1+ia\mathbf{Q}/2}\right]\left[\frac{1-ia^*\mathbf{Q}/2}{1+ia^*\mathbf{Q}/2}\right], \end{aligned} \tag{A3}$$

with the error term being $i\mathbf{Q}^5/720$ and with $a = (1+i/\sqrt{3})/2$. The second line shows the best way to evaluate this approximation as two Crank-Nicolson steps.

The Crank-Nicolson step is implemented as follows:

$$\frac{1-i\mathbf{M}\delta t/2}{1+i\mathbf{M}\delta t/2}\vec{b} = \frac{2}{1+i\mathbf{M}\delta t/2}\vec{b} - \vec{b} \equiv \vec{x} - \vec{b}. \tag{A4}$$

The vector $\vec{x}$ is obtained by solving a linear equation $\mathbf{A}\vec{x} = \vec{b}$ where the only nonzero elements of $\mathbf{A} = (1+i\boldsymbol{M}\delta t/2)/2$ are on the diagonal and on the edges $A_{0\nu}$ and $A_{\nu 0}$. This sparse matrix equation can be solved as

$$\left(A_{00} - \sum_\nu A_{0\nu}A_{\nu\nu}^{-1}A_{\nu 0}\right)x_0 = b_0 - \sum_\nu A_{0\nu}A_{\nu\nu}^{-1}b_\nu, \tag{A5a}$$

$$A_{\nu\nu}x_\nu = b_\nu - A_{\nu 0}x_0, \tag{A5b}$$

with the number of operations being of order N. If the equations are time-independent, various combinations can be calculated and stored, greatly increasing the speed of the calculation (for example, the combination $A_{0\nu}A_{\nu\nu}^{-1}$ and the term in parentheses).

When numerically implementing the equations that have adiabatically eliminated the cavity mode (such as (25)), the matrix solution of the Crank-Nicolson approximation is still sparse. In this case, we use the Sherman-Morrison formula (Ref. 27).

Appendix B: Continuum Limit of Oscillator Equations

Here we derive the continuum limit of the oscillator equations

$$i\dot{b}_0 = -\left(\Delta + i\frac{\Gamma}{2}\right)b_0 + \sum_{j=1}^{N} b_j\eta_j^*, \tag{B1a}$$

$$i\dot{b}_j = \left(\Delta_j - i\frac{\gamma}{2}\right)b_j + b_0\eta_j. \tag{B1b}$$

We order the oscillators so that $\Delta_{j+1} > \Delta_j$ for all $j = 1,\ldots,N$. Let ψ be a continuous detuning variable. We take a lattice of N points in ψ such that $\psi_j = \Delta_j$ and define functions $b(\psi)$ and $\eta(\psi)$ such that $b(\psi_j,t) = b_j(t)$ and $\eta(\psi_j,t) = \eta_j(t)$. This lets us rewrite (B1) in terms of ψ as

$$i\dot{b}_0 = -\left(\Delta + i\frac{\Gamma}{2}\right)b_0 + \sum_j b(\psi_j,t)\eta^*(\psi_j,t), \tag{B2a}$$

$$i\frac{\partial}{\partial t}b(\psi_j,t) = \left(\psi_j - i\frac{\gamma}{2}\right)b(\psi_j,t) + b_0\eta(\psi_j,t). \tag{B2b}$$

The continuum limit $N\to\infty$ of (B2b) is obtained when the lattice of points ψ_j becomes dense enough to be replaced with the continuous variable ψ.

The continuum limit of the sum

$$\sum_{j=1}^{N} b(\psi_j,t)\eta^*(\psi_j,t) \tag{B3}$$

is more subtle. We can multiply and divide by $\Delta\psi_j = \psi_{j+1} - \psi_j$ inside the sum,

$$\sum_{j=1}^{N} b(\psi_j,t)\eta^*(\psi_j,t)\Delta\psi_j/\Delta\psi_j. \tag{B4}$$

We would like to pull $1/\Delta\psi_j$ outside the sum so that the limit of what remains would be a Riemann integral.

Each ψ_j is sampled from the same probability distribution $P(\psi)$ ($\int P(\psi)\,\mathrm{d}\psi = 1$). We can look for an average value of $\Delta\psi_j$ to pull out of the sum. Consider a small interval $\delta\psi_j$ containing ψ_j. The average number of points that fall in this interval is approximately $n = NP(\psi_j)\delta\psi_j$. The average spacing of points is $\Delta\psi_j = \delta\psi_j/n = 1/(NP(\psi_j))$. So $1/\Delta\psi_j$ is (on average) $NP(\psi_j)$. This lets us rewrite the sum as

$$N\sum_{j=1}^{N} b(\psi_j,t)\eta^*(\psi_j,t)P(\psi_j)\Delta\psi_j, \tag{B5}$$

which in the large N limit becomes the integral

$$N\int \mathrm{d}\psi b(\psi,t)\eta^*(\psi,t)P(\psi). \tag{B6}$$

Thus the continuum limit of the equations (B1) is

$$i\dot{b}_0 = -\left(\Delta + i\frac{\Gamma}{2}\right)b_0 + N\int \mathrm{d}\psi b(\psi,t)\eta^*(\psi,t)P(\psi), \tag{B7a}$$

$$i\frac{\partial}{\partial t}b(\psi,t) = \left(\psi - i\frac{\gamma}{2}\right)b(\psi,t) + \eta(\psi,t)b_0. \tag{B7b}$$

We can find the dispersion relation for this system by taking $b_0, b \sim \exp(-i\alpha t)$:

$$\alpha + \Delta + i\frac{\Gamma}{2} = N\int \mathrm{d}\psi P(\psi)\frac{|\eta(\psi,t)|^2}{\alpha - \psi + i\frac{\gamma}{2}}. \tag{B8}$$

If we take η = constant and use a uniform $P(\psi) = (\delta\Omega\sqrt{(12)})^{-1}$ between $\Delta \pm \sqrt{3}\delta\Omega$, we get the dispersion relation

$$\alpha + \Delta + i\frac{\Gamma}{2} = \frac{N|\eta|^2}{\delta\Omega\sqrt{12}}\ln\left(\frac{\alpha - \Delta + \delta\Omega\sqrt{3} - i\gamma/2}{\alpha - \Delta - \delta\Omega\sqrt{3} - i\gamma/2}\right). \tag{B9}$$

Appendix C: Summary of Symbols and Definitions

Quantity	Symbol	Definition
Mode frequency	ω	—
Mode function	$\boldsymbol{h}(\boldsymbol{x})$	$\boldsymbol{A}_{\rm cav} = \frac{mc}{e}\sum_\alpha a_\alpha \boldsymbol{h}_\alpha(\boldsymbol{x})e^{-i\omega_\alpha t} + \text{c.c}$
Mode volume	V	$\int \mathrm{d}^3\boldsymbol{x}\boldsymbol{h}^*_{\alpha'}\cdot\boldsymbol{h}_\alpha = V_\alpha\delta_{\alpha'\alpha}$
j'th electron cyclotron frequency	Ω_j	$\Omega_j = eB_{\rm ext}(\boldsymbol{x}_j)/m$
Average cyclotron frequency	$\bar{\Omega}$	$\bar{\Omega} = \sum_j \Omega_j/N$
Cyclotron frequency spread	$\delta\Omega$	$\delta\Omega = \sqrt{\sum_j(\Omega_j-\bar{\Omega})^2/N}$
Electron bounce (axial) frequency	$\omega_{b,j}$	—
Average bounce (axial) frequency	$\bar{\omega}_b$	$\bar{\omega}_b = \sum_j \omega_{b,j}/N$
Axial frequency spread	$\delta\omega_b$	$\delta\omega_b = \sqrt{\sum_j(\omega_{b,j}-\bar{\omega}_b)^2/N}$
Axial frequency full spread	$\widehat{\delta\omega}_b$	$\widehat{\delta\omega}_b = \sqrt{12}\,\delta\omega_b$ (uniform distribution)
Cyclotron detunings	Δ_j	$\Delta_j = \Omega_j - \bar{\Omega}$
Cavity detuning	Δ	$\Delta = \bar{\Omega} - \omega$
Cavity mode decay rate	Γ	(due to resistive effect of the walls)
Cyclotron mode decay rate	γ	(due to coupling to traveling modes)
Spherical basis vectors	$\hat{\mathbf{e}}_{+,0,-}$	$\hat{\mathbf{e}}_\pm = (\pm\hat{\mathbf{x}} - i\hat{\mathbf{y}})/\sqrt{2}, \hat{\mathbf{e}}_0 = \hat{\mathbf{z}}$
Components of spherical basis vectors	$v_\pm, v_z$	$v_\pm = \hat{\mathbf{e}}^*_\pm\cdot\boldsymbol{v} = (\pm v_x + iv_y)/\sqrt{2}$, $v_z = \hat{\mathbf{e}}^*_0\cdot\boldsymbol{v}$
Cavity mode amplitudes	$a, \bar{a}, b_0, \tilde{b}_0$	$\bar{a} = \tilde{b}_0 = ae^{i\Delta t} = b_0 e^{(i\Delta-\gamma/2)t}$
Cyclotron velocities	$v_{j\pm}, \tilde{v}_{j\pm}, b_j, \tilde{b}_j$	$\tilde{v}_\pm = v_\pm e^{\mp i\bar{\Omega}t}$, $\tilde{b}_j = e\tilde{v}_{j-}/(\omega c\sqrt{2mV\varepsilon_0}) = b_j e^{(i\Delta-\gamma/2)t}$
Cavity coupling parameter	η_j, η	$\eta_j = eh_-(\boldsymbol{x}_j)/\sqrt{2mV\varepsilon_0}$ (use η when all η_j same)
Single electron frequency shift	$\delta\omega$	$\delta\omega = (4\|\eta\|^2\Delta/\Gamma^2)/[1+(2\Delta/\Gamma)^2]$
Single electron decay rate	Γ_1	$\Gamma_1 = (4\|\eta\|^2/\Gamma)/[1+(2\Delta/\Gamma)^2]$
Collective mode decay rate in uniform magnetic field	Γ_N	$\Gamma_N = \frac{\Gamma}{2}\left(1-\sqrt{1-4N\Gamma_1/\Gamma}\right), 4N\Gamma_1 < \Gamma$; $\Gamma_N = \Gamma/2,, 4N\Gamma_1 > \Gamma$
Dimensionless quantities	$\tau, \delta\tilde{\Omega}, \tilde{\Delta}, \tilde{\Gamma}$,etc.	$\tau = \eta t$, $\delta\tilde{\Omega} = \delta\Omega/\eta$, $\tilde{\Delta} = \Delta/\eta$, $\tilde{\Gamma} = \Gamma/\eta$, etc
Normalized average frequency spacing	χ, ζ	$\chi = (\delta\tilde{\Omega})\tilde{\Gamma}/N = 4\delta\Omega/(N\Gamma_1) = 2\zeta/\sqrt{3}$
Critical frequency spacing	$\chi_{\rm crit}$	$\chi_{\rm crit} = \tilde{\Gamma}^2/N = 4\Gamma/(N\Gamma_1)$
Normalized axial frequency spacing	$\chi_{\rm axial}$	$\chi_{\rm axial} = \delta\omega_b/(N\Gamma_1)$
Collision rate	$\Gamma_{\rm col}$	—
Normalized collision rate	$\gamma_{\rm col}$	$\gamma_{\rm col} = \Gamma_{\rm col}/(N\Gamma_1)$

Table I. Summary of symbols and definitions used for key quantities.

REFERENCES

[1]J. R. Danielson, D. H. E. Dubin, R. G. Greaves, and C. M. Surko, Rev. Mod. Phys. **87**, 247 (2015).
[2]M. Ahmadi, B. X. R. Alves, C. J. Baker, W. Bertsche, E. Butler, A. Capra, C. Carruth, C. L. Cesar, M. Charlton, S. Cohen, R. Collister, S. Eriksson, A. Evans, N. Evetts, J. Fajans, T. Friesen, M. C. Fujiwara, D. R. Gill, A. Gutierrez, J. S. Hangst, W. N. Hardy, M. E. Hayden, C. A. Isaac, A. Ishida, M. A. Johnson, S. A. Jones, S. Jonsell, L. Kurchaninov, N. Madsen, M. Mathers, D. Maxwell, J. T. K. McKenna, S. Menary, J. M. Michan, T. Momose, J. J. Munich, P. Nolan, K. Olchanski, A. Olin, P. Pusa, C. Ø. Rasmussen, F. Robicheaux, R. L. Sacramento, M. Sameed, E. Sarid, D. M. Silveira, S. Stracka, G. Stutter, C. So, T. D. Tharp, J. E. Thompson, R. I. Thompson, D. P. van der Werf, and J. S. Wurtele, Nature Communications **8**, 681 (2017).
[3]F. Robicheaux and J. Fajans, Journal of Physics B: Atomic, Molecular and Optical Physics **40**, 3143 (2007).
[4]B. R. Beck, J. Fajans, and J. H. Malmberg, Physics of Plasmas **3**, 1250 (1996).
[5]M. E. Glinsky, T. M. O'Neil, M. N. Rosenbluth, K. Tsuruta, and S. Ichimaru, Physics of Fluids B: Plasma Physics **4**, 1156 (1992).
[6]A. Povilus, N. DeTal, L. Evans, N. Evetts, J. Fajans, W. Hardy, E. Hunter, I. Martens, F. Robicheaux, S. Shanman, *et al.*, Physical Review Letters **117**, 175001 (2016).
[7]T. O'Neil, The Physics of Fluids **23**, 725 (1980).
[8]E. M. Purcell, H. C. Torrey, and R. V. Pound, Physical Review **69**, 37 (1946).
[9]G. Gabrielse and H. Dehmelt, Phys. Rev. Lett. **55**, 67 (1985).
[10]N. Evetts, I. Martens, D. Bizzotto, D. Longuevergne, and W. Hardy, Review of Scientific Instruments **87**, 104702 (2016).
[11]E. D. Hunter, N. Evetts, J. Fajans, W. N. Hardy, H. Landsberger, R. Mcpeters, and J. S. Wurtele, Physics of Plasmas **25**, 011602 (2018).
[12]E. Hunter, *Cavity and Microwave Experiments on Electron Plasma*, Ph.D. thesis, University of California at Berkeley (2020).
[13]R. Sáez-Blázquez, J. Feist, F. García-Vidal, and A. Fernández-Domínguez, Physical Review A **98**, 013839 (2018).
[14]D. Plankensteiner, C. Sommer, M. Reitz, H. Ritsch, and C. Genes, Physical Review A **99**, 043843 (2019).
[15]M. Reitz, C. Sommer, and C. Genes, Physical Review Letters **122**, 203602 (2019).
[16]S. Girvin, M. Devoret, and R. Schoelkopf, Physica Scripta **2009**, 014012 (2009).
[17]Y. Sun and P.-X. Chen, Optica **5**, 1492 (2018).
[18]S. Kumar, J. Sheng, J. A. Sedlacek, H. Fan, and J. P. Shaffer, Journal of Physics B: Atomic, Molecular and Optical Physics **49**, 064014 (2016).
[19]A. Shalabney, J. George, J. a. Hutchison, G. Pupillo, C. Genet, and T. W. Ebbesen, Nature Communications **6**, 5981 (2015).
[20]E. Ott and T. M. Antonsen, Chaos: An Interdisciplinary Journal of Nonlinear Science **18**, 037113 (2008).
[21]D. Golomb, D. Hansel, B. Shraiman, and H. Sompolinsky, Physical Review A **45**, 3516 (1992).
[22]Y. Kuramoto and I. Nishikawa, Journal of Statistical Physics **49**, 569 (1987).
[23]S. H. Strogatz and R. E. Mirollo, Journal of Statistical Physics **63**, 613 (1991).
[24]W. M. Itano, J. C. Bergquist, J. J. Bollinger, and D. J. Wineland, Physica Scripta **1995**, 106 (1995).
[25]R. H. Dicke, Phys. Rev. **93**, 99 (1954).
[26]K. Baumann, C. Guerlin, F. Brennecke, and T. Esslinger, Nature **464**, 1301 (2010).
[27]W. H. Press, S. A. Teukolsky, W. T. Vetterling, and B. P. Flannery, *Numerical recipes in Fortran 77: the art of scientific computing*, Vol. 2 (Cambridge university press Cambridge, 1992).

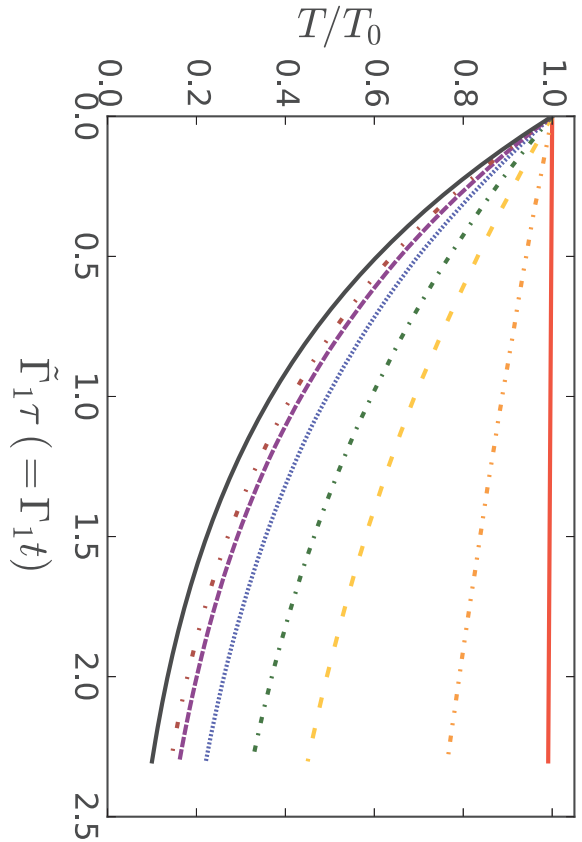

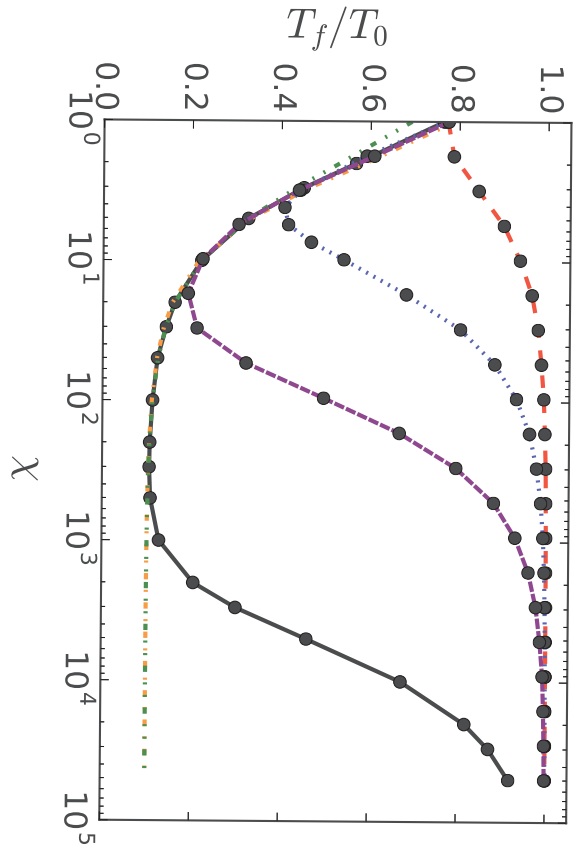

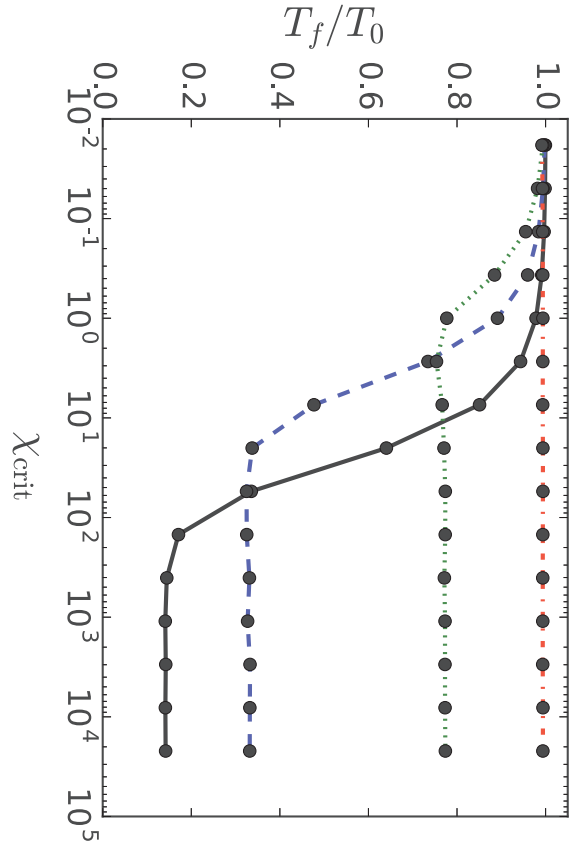

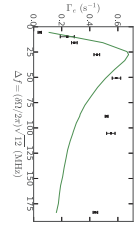

PLEASE CITE THIS ARTICLE AS DOI: 10.1063/5.0012756

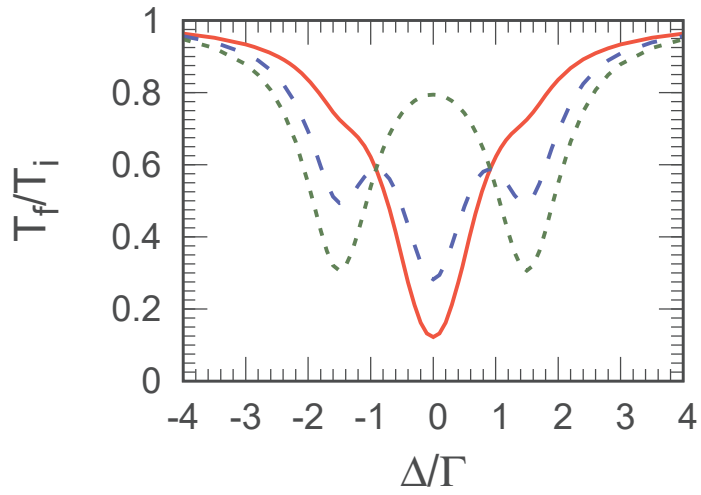

PLEASE CITE THIS ARTICLE AS DOI: 10.1063/5.0012756

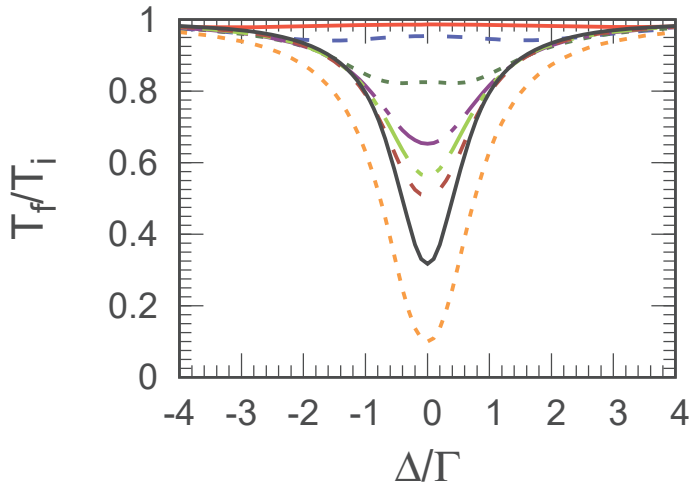

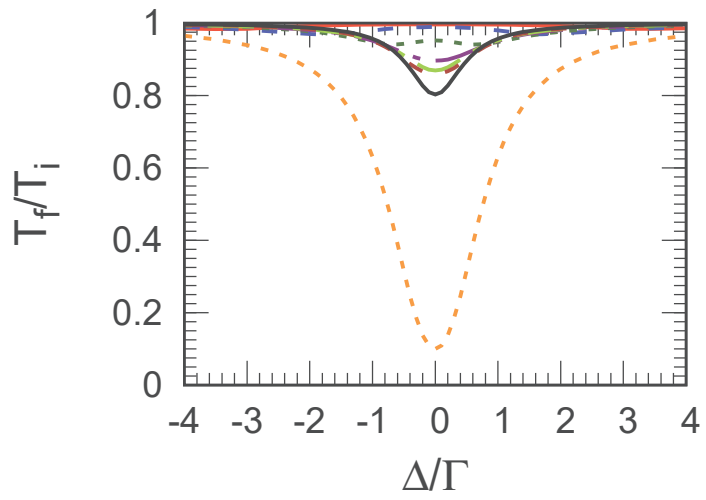

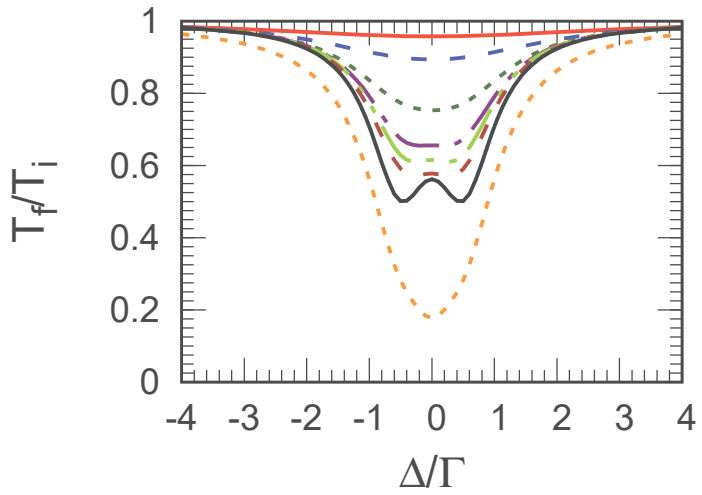

PLEASE CITE THIS ARTICLE AS DOI: 10.1063/5.0012756